





**UNIVERSIDAD DE INVESTIGACIÓN DE  
TECNOLOGÍA EXPERIMENTAL YACHAY**

**Escuela de Ciencias Químicas e Ingeniería**

**TÍTULO: Possibility of reusing industrial waste to  
synthesize a depolluting silica monolith through HIPE  
method: an experimental and theoretical study**

Trabajo de integración curricular presentado como requisito para la  
obtención de título de Química

**Autor:**

Alexander Tipán

**Tutora:**

Ph.D. Alicia Sommer

**Co-tutor:**

Ph.D. Thibault Terencio

Urququí, Octubre 2020



Urcuquí, 7 de octubre de 2020

**SECRETARÍA GENERAL**  
(Vicerrectorado Académico/Cancillería)  
**ESCUELA DE CIENCIAS QUÍMICAS E INGENIERÍA**  
**CARRERA DE QUÍMICA**  
**ACTA DE DEFENSA No. UITEY-CHE-2020-00053-AD**

A los 7 días del mes de octubre de 2020, a las 16:00 horas, de manera virtual mediante videoconferencia, y ante el Tribunal Calificador, integrado por los docentes:

<b>Presidente Tribunal de Defensa</b>	Dra. VARELA SALAZAR, SOLMAR ALEXANDRA , Ph.D.
<b>Miembro No Tutor</b>	Dra. LOPEZ GONZALEZ, FLORALBA AGGENY , Ph.D.
<b>Tutor</b>	Dra. SOMMER MARQUEZ, ALICIA ESTELA , Ph.D.

El(la) señor(ita) estudiante TIPAN QUIHPE, ALEXANDER MAURICIO, con cédula de identidad No. 1723765507, de la ESCUELA DE CIENCIAS QUÍMICAS E INGENIERÍA, de la Carrera de QUÍMICA, aprobada por el Consejo de Educación Superior (CES), mediante Resolución RPC-SO-39-No.456-2014, realiza a través de videoconferencia, la sustentación de su trabajo de titulación denominado: POSSIBILITY OF REUSING INDUSTRIAL WASTE TO SYNTHESIZE A DEPOLLUTING SILICA MONOLITH THROUGH HIPE METHOD: AN EXPERIMENTAL AND THEORETICAL STUDY, previa a la obtención del título de QUÍMICO/A.

El citado trabajo de titulación, fue debidamente aprobado por el(los) docente(s):

<b>Tutor</b>	Dra. SOMMER MARQUEZ, ALICIA ESTELA , Ph.D.
<b>Co - Tutor</b>	Dr. TERCICIO THIBAUT , Ph.D.

Y recibió las observaciones de los otros miembros del Tribunal Calificador, las mismas que han sido incorporadas por el(la) estudiante.

Previamente cumplidos los requisitos legales y reglamentarios, el trabajo de titulación fue sustentado por el(la) estudiante y examinado por los miembros del Tribunal Calificador. Escuchada la sustentación del trabajo de titulación a través de videoconferencia, que integró la exposición de el(la) estudiante sobre el contenido de la misma y las preguntas formuladas por los miembros del Tribunal, se califica la sustentación del trabajo de titulación con las siguientes calificaciones:

Tipo	Docente	Calificación
Miembro Tribunal De Defensa	Dra. LOPEZ GONZALEZ, FLORALBA AGGENY , Ph.D.	10,0
Presidente Tribunal De Defensa	Dra. VARELA SALAZAR, SOLMAR ALEXANDRA , Ph.D.	10,0
Tutor	Dra. SOMMER MARQUEZ, ALICIA ESTELA , Ph.D.	10,0

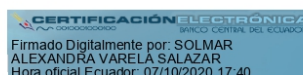
Lo que da un promedio de: **10 (Diez punto Cero)**, sobre 10 (diez), equivalente a: **APROBADO**

Para constancia de lo actuado, firman los miembros del Tribunal Calificador, el/la estudiante y el/la secretario ad-hoc.

Certifico que *en cumplimiento del Decreto Ejecutivo 1017 de 16 de marzo de 2020, la defensa de trabajo de titulación (o examen de grado modalidad teórico práctica) se realizó vía virtual, por lo que las firmas de los miembros del Tribunal de Defensa de Grado, constan en forma digital.*

TIPAN QUIHPE, ALEXANDER MAURICIO  
Estudiante

Dra. VARELA SALAZAR, SOLMAR ALEXANDRA , Ph.D.  
Presidente Tribunal de Defensa



Dra. SOMMER MARQUEZ, ALICIA ESTELA , Ph.D.  
**Tutor**

ALICIA  
ESTELA  
SOMMER  
MARQUEZ


Firmado digitalmente por ALICIA ESTELA SOMMER MARQUEZ  
Fecha: 2020.10.08 08:09:35 -05'00"

Dra. LOPEZ GONZALEZ, FLORALBA AGGENY , Ph.D.  
**Miembro No Tutor**



Firmado electrónicamente por:  
FLORALBA AGGENY  
LOPEZ GONZALEZ

CIFUENTES TAFUR, EVELYN CAROLINA  
**Secretario Ad-hoc**



Firmado electrónicamente por:  
EVELYN CAROLINA  
CIFUENTES TAFUR

## AUTORÍA

Yo, **ALEXANDER MAURICIO TIPÁN QUISHPE**, con cédula de identidad 1723765507, declaro que las ideas, juicios, valoraciones, interpretaciones, consultas bibliográficas, definiciones y conceptualizaciones expuestas en el presente trabajo; así cómo, los procedimientos y herramientas utilizadas en la investigación, son de absoluta responsabilidad de el/la autor (a) del trabajo de integración curricular. Así mismo, me acojo a los reglamentos internos de la Universidad de Investigación de Tecnología Experimental Yachay.

Urcuquí, Octubre 2020



---

Alexander Mauricio Tipán Quishpe  
CI: 1723765507



## AUTORIZACIÓN DE PUBLICACIÓN

Yo, **ALEXANDER MAURICIO TIPÁN QUISHPE**, con cédula de identidad 1723765507, cedo a la Universidad de Investigación de Tecnología Experimental Yachay, los derechos de publicación de la presente obra, sin que deba haber un reconocimiento económico por este concepto. Declaro además que el texto del presente trabajo de titulación no podrá ser cedido a ninguna empresa editorial para su publicación u otros fines, sin contar previamente con la autorización escrita de la Universidad.

Asimismo, autorizo a la Universidad que realice la digitalización y publicación de este trabajo de integración curricular en el repositorio virtual, de conformidad a lo dispuesto en el Art. 144 de la Ley Orgánica de Educación Superior.

Urcuquí, Octubre 2020.



---

Alexander Mauricio Tipán Quishpe

CI: 1723765507





# *Dedication*

Dedicated to my lovely parents, Rosa Quishpe and Rene Tipán, for their full support in my decisions.

Alexander Mauricio Tipán Quishpe



## *Acknowledgements*

First and foremost, I would like to express my deep and sincere gratitude to my parents Rosa and Rene for their love, prayers and sacrifices for educating and preparing me to my future. I also thanks for my brother Hugo to encouraged me to overcome difficulties and achieve my goals.

I would like to express my special thanks of gratitude to my advisor Ph.D. Alicia Sommer-Marquez, researcher at YachayTech University for giving me the opportunity to do research and provinding invaluable guidance throughout this work. As well as my co-advisor Ph.D. Thibault Terencio for his guidance in theoretical and experimental part of this work. Besides, I would like to thank the rest of my thesis committe: Ph.D. Solmar Varela and Ph.D. Floralba López, for the time taken in their insightful comments.

I am extending my thanks to Ph.D. Edward E. Ávila (UITEY, Urcuquí-Ecuador) for his collaboration with PXRD data collection. I also thank to SENESCYT - INEDITA (grant PIC-18-INE-YACHAY-001) for partial financial support for the use of powder diffractometer Miniflex-600, Rigaku, with a D/tex Ultra2 detector. Also, I thank to Msc. Elizabeth Mariño, lab technician of School of Earth Science, Energy and Environmental, for her guidance in the use of SkyScan 2211 Nano-Computed Tomography.

I also thank all the staff of Yachay Tech University who during the my instance in the campus have supported me in several ways to complete this thesis successfully. I express my special thanks for Ph.D. Francisco Alvarez and Tomoko Kawamura for their unconditional support in the learning of foreign language and scholar skills.

I would like to say thanks to all my friends, teachers, and research colleagues for the cooperation, teaching and fellowship that extended me during these years.

Finally, my thanks go to all the people who have supported me to complete my undergraduate thesis directly or indirectly.

Alexander Mauricio Tipán Quishpe



## Resumen

Los monolitos de sílice son materiales porosos con una estructura característica conectada y un esqueleto en forma de malla de orden mesoporoso que se pueden usar para descontaminar varios residuos tóxicos del agua. A través de la síntesis de emulsión de alta fase interna (HIPE), se pueden obtener monolitos con porosidad jerarquizada. Este tipo de materiales tienen macroporosos en conjunto con mesoporosos dando como resultado un incremento en vías más accesibles para una mejor difusión combinada con una área específica alta, muy importante en muchas aplicaciones relacionadas con la adsorción y la transferencia de masa. Debido a su porosidad jerarquizada, los monolitos mejoraron la eficiencia del lecho en columna para procesos continuos, y la selectividad, coeficiente de distribución y cinética de intercambio en procesos por lotes. Además, los monolitos pueden ser funcionalizados con metales, entre otras cosas, con el fin de obtener propiedades especiales para aplicaciones en catálisis y sorción. En este proyecto se utilizó un bien establecido y sencillo método de síntesis para la obtención de monolitos de sílice con porosidad jerarquiza realizado por emulsiones de alto contenido de fase interna (HIPE). Se utilizó aceite de cocina reciclado como fase interna y se funcionalizaron con cobre como modelo de agente contaminante en agua proveniente de desechos industriales para obtener materiales que pueden ser empleados como bactericidas para la descontaminación del agua potable. La morfología, estructura de los átomos y presencia del metal en la red del monolito se han logrado determinar de acuerdo a los resultados dados por microscopía electrónica de barrido (MEB), nanotomografía computarizada (nano-CT), difracción de rayos X (DRX), espectroscopías infrarroja de reflexión total atenuada (ATRFTIR) y reflectancia difusa de UV-Vis (DR-UV-Vis). También se realizaron simulaciones teóricas para confirmar que el cobre puede ser parte de la red de sílice ya que claramente se muestra, a través de los datos obtenidos, que el cobre se comporta como el silicio al construir la red y prefiere ir a entornos con presencia de oxígeno. Finalmente, se realizó una prueba experimental antibacteriana con los monolitos funcionalizados con cobre en muestras de agua provenientes de fuentes naturales. Los resultados sugieren que es un material descontaminante efectivo contra Coliformes Totales y *E. Coli* para las muestras de agua tratadas provenientes del hidrante de Santa Cruz - Galápagos.

**Palabras clave:** Monolito, Silice, HIPE, Quantum espresso



## *Abstract*

Silica monoliths are porous materials with a characteristic structure connected with a mesh-like skeleton of mesoporous order which can be used to decontaminate several toxic residues from water. Through High Internal Phase Emulsion (HIPE) synthesis, hierarchical monoliths can be obtained. This type of materials have macroporous combined with mesoporous which increase accessible diffusion pathways combined with high surface area, very important in many applications dealing with adsorption and mass transfer. Due to their hierarchically porous architecture, monoliths improved the bed efficiency in column for continuous processes, and the selectivity, distribution coefficient and exchange kinetics in batch processes. Moreover, monoliths can be functionalized with metals, among others, in order to gain special properties for catalysis and sorption applications. In this project, a facile synthesis method of high internal phase emulsion (HIPE) for obtaining hierarchical silica monoliths, using recycled cooking oil and functionalization with copper was performed. The morphology, structure of the atoms, and presence of the metal in the network of the monolith have been achieved according to the results given by Scanning Electron Microscopy (SEM), nano-Computed Tomography (nano-CT), X-Ray Powder Diffraction (XRD), Attenuated Total Reflection Infrared Spectroscopy (ATR-FTIR) and Diffuse Reflectance UV-Vis (DRS-UV-Vis). Theoretical Simulations were also carried out to confirm that copper can be part of the silica framework because is clearly shown that copper behaves as silicon when building the network and prefers to go to oxygen-presence environments. In addition, an antibacterial experimental test was performed with the functionalized monoliths as a possibility to decontaminate drinking water. The given results suggest an effective depolluting material against Total Coliforms and *E. Coli* for the tap water samples of the hydrant from Santa Cruz- Galapagos.

**Keywords:** Monolith, Silica, High Internal Phase Emulsion, Quantum espresso





# Contents

<b>Acknowledgements</b>	<b>xi</b>
<b>Resumen</b>	<b>xiii</b>
<b>Abstract</b>	<b>xv</b>
<b>List of Figures</b>	<b>xxi</b>
<b>List of Tables</b>	<b>xxv</b>
<b>1 Background</b>	<b>1</b>
1.1 Porous Materials . . . . .	1
1.1.1 Characteristics and properties of porous materials . . . . .	2
Zeolites . . . . .	2
Silica pure chabazite . . . . .	3
1.1.2 Mechanism of synthesis of zeolites and pure silica chabazite . . . . .	3
Zeolites . . . . .	3
Pure silica chabazite . . . . .	4
1.2 Monolithic porous materials . . . . .	5
1.2.1 Monolithic disks . . . . .	7
Mechanism of synthesis . . . . .	7
Applications . . . . .	8
1.2.2 Rod monoliths . . . . .	8
Mechanism of synthesis . . . . .	8
Applications . . . . .	9
1.3 Hierarchical porous materials . . . . .	9
1.3.1 Types of hierarchical porous materials . . . . .	10
1.3.2 Mechanism of synthesis . . . . .	11
1.3.3 Applications . . . . .	13
1.4 Emulsions as soft templates . . . . .	14
1.4.1 Types of emulsions . . . . .	15
1.4.2 High Internal Phase Emulsions . . . . .	15
1.5 Poloxamers, an interesting surfactant with tunable properties . . . . .	16

1.5.1	Types of poloxamers . . . . .	17
1.5.2	Applications of poloxamers . . . . .	18
1.5.3	Pluronic® P123 . . . . .	18
1.6	Applications of hierarchical silica monoliths . . . . .	18
1.7	Theoretical simulations as a tool to study porous materials . . . . .	19
1.8	Drinking water . . . . .	20
1.8.1	Regulation of drinking water in Ecuador . . . . .	21
<b>2</b>	<b>Problem Statement</b>	<b>25</b>
2.1	Objectives . . . . .	25
2.1.1	General Objective . . . . .	25
2.1.2	Specific Objectives . . . . .	25
<b>3</b>	<b>Methodology</b>	<b>27</b>
3.1	Synthesis of hierarchical porous silica monolith . . . . .	27
3.1.1	Materials and reagents . . . . .	27
3.1.2	Experimental procedure . . . . .	27
3.2	Characterization Techniques . . . . .	29
3.2.1	Scanning Electron Microscopy . . . . .	29
3.2.2	X-ray Nano-Computed Tomography . . . . .	30
3.2.3	X-Ray Powder Diffraction Spectroscopy . . . . .	31
3.2.4	Attenuated Total Reflection FTIR Spectroscopy . . . . .	33
3.2.5	Diffuse Reflectance UV-Vis Spectroscopy . . . . .	34
3.3	Theoretical simulations . . . . .	35
3.3.1	Quantum Espresso . . . . .	35
	Input file . . . . .	35
	Run a File . . . . .	36
3.3.2	Computational methods . . . . .	36
3.4	Antibacterial analysis . . . . .	37
3.4.1	Materials and Reagents . . . . .	37
3.4.2	Experimental procedure . . . . .	38
<b>4</b>	<b>Results and Discussion</b>	<b>41</b>
4.1	Silica monoliths through HIPE method . . . . .	41
4.1.1	Scanning Electron Microscope . . . . .	41
4.1.2	X-ray Nano-Computed Tomography after calcination . . . . .	42
4.2	Use of recycled oil as oleic phase for monolith synthesis . . . . .	43
4.3	Copper functionalization of monolith . . . . .	44

4.3.1	Physical features of the functionalized silica monolith after calcination . . . . .	44
4.3.2	X-Ray Powder Diffraction . . . . .	45
4.3.3	Diffuse Reflectance of UV-Vis Spectroscopy (DRS-UV-Vis) . .	47
4.3.4	Attenuated Total Reflection FTIR spectroscopy . . . . .	48
4.3.5	Conclusions on the experimental synthesis and characterization	49
4.4	Theoretical simulations . . . . .	49
4.5	Antibacterial test . . . . .	52
4.5.1	Material resistance after the test evaluated by DRS-UV-Vis . .	56
<b>5</b>	<b>Conclusions and future work</b>	<b>57</b>
<b>A</b>	<b>Data analysis</b>	<b>59</b>
A.1	Crystalline structure of CuO nanoparticles . . . . .	59
<b>B</b>	<b>Computational files</b>	<b>61</b>
B.1	Input codes for simulations of copper adsorption on silica and pure chabazite surfaces . . . . .	61
	<b>Bibliography</b>	<b>65</b>



# List of Figures

1.1	Illustration of crystalline porous structure of unit cell of Analcime zeolite performed with XCrySDen® (O:red, Si: light blue) . . . . .	2
1.2	Illustration of crystalline structure of chabazite and double six member-rings made with xCrySDen® (O: red, Si: light blue). . . . .	3
1.3	Hydrothermal zeolite synthesis. The starting materials are converted by an aqueous mineralising medium ( $OH^-$ and/or $F^-$ ) into the crystalline product whose microporosity is defined by the crystal structure [8]. . . . .	4
1.4	Hydrothermal pure silica chabazite synthesis based on the work by Dang [16]. . . . .	5
1.5	The structure of a rod monolithic silica with the bimodal pore structure.	6
1.6	Image of disk monolithic silica used in HPLC columns [21]. . . . .	7
1.7	Image of the silica rod columns with different size . . . . .	8
1.8	Illustration of hierarchical structured porous natural materials, placed alongside the length scale according to their critical dimensions. . . .	10
1.9	Hard templating method scheme . . . . .	11
1.10	Methodology of the primary (left) and secondary (right) soft templating methods. . . . .	12
1.11	Illustration of the emulsion formation and stabilization [55]. . . . .	14
1.12	Illustration of the chemical structure of a poloxamer [68]. . . . .	16
1.13	Pluronic® grid (colour code: physical state of copolymers under ambient conditions: green = liquid; red = paste; orange = flake) [69]. . .	17
1.14	Water cycle in the island and the contamination of groundwater sources [92]. . . . .	22
3.1	General scheme of the synthesis of silica monoliths. . . . .	28
3.2	Schematic diagram of the core components of a SEM microscope [101].	30
3.3	Illustrations of laboratory micro-CT scanner geometries [104]. . . . .	31
3.4	A Bragg-Brentano geometry based diffractometer [107]. . . . .	32
3.5	A multiple reflection ATR system [111]. . . . .	34

3.6	Illustration of projection of the spectrometer beam into the sample where it is reflected, scattered and transmitted through the sample [116]. . . . .	35
3.7	Input file for a <i>CuO</i> molecule with the structure for a non self calculation performed in Text editor. . . . .	37
3.8	A scheme of the multiparameter analysis and microbiological test of the HCWS. a) Experimental procedure of the blank sample and b) Experimental procedure of the control water samples with "MonOilCu" (A, B, and C). . . . .	39
4.1	a) Image of silica monolith by HIPE non calcined "Mon1". b) and c) SEM images of silica monolith "Mon1" at 2700x and 6900x magnification, respectively. d) Distribution of the porosity in the "Mon1" performed in ImageJ. . . . .	42
4.2	Images of a) calcined silica monolith synthesized by HIPE "Mon2" and b) nano-computed tomography of "Mon2" where macroporous is visible. . . . .	43
4.3	a) Infrared spectrum of silica monolith "Mon1" in the spectral range associated with bonds of amorphous silica with the respective bands and b) Infrared spectrum of silica monolith "MonOil" in the spectral range associated with bonds of amorphous silica. . . . .	44
4.4	Images of the functionalized monoliths with copper, a) it was aged by seven days and b) aged seven days and calcined in the muffle furnace with the ramp of 500°C. . . . .	45
4.5	XRD diffractograms of the silica monoliths. a) XRD spectra of "MonOil" with an amorphous peak, b) XRD spectra of "MonOilCu" which shows a <i>CuO</i> peaks, c) Offsets of XRD spectrum of "MonOil" and "MonOilCu" and d) Theoretical XRD spectrum of <i>CuO</i> obtained from GDIS software. . . . .	46
4.6	The UV-Vis diffuse reflectance spectra of "MonCu" and "MonOilCu" silica monoliths. . . . .	48
4.7	Infrared spectrum of silica monolith "MonOilCu" in the spectral range associated with bonds of amorphous silica . . . . .	49
4.8	A ball-and-stick model for copper absorbed of pure silica surface  100  interface ( <i>Si</i> : light blue, and <i>Cu</i> : orange). . . . .	50
4.9	A ball-and-stick model for copper absorbed at left position of pure silica chabazite unit cell surface  100  interface ( <i>O</i> : red, <i>Si</i> : light blue, and <i>Cu</i> : orange). . . . .	51

4.10	A ball-and-stick model for copper absorbed at center position of pure silica chabazite unit cell surface  100  interface (O: red, Si: light blue, and Cu: orange). . . . .	51
4.11	A ball-and-stick model for copper absorbed at right position of pure silica chabazite unit cell surface  100  interface (O: red, Si: light blue, and Cu: orange). . . . .	52
4.12	Image of the membrane filtration result from the hydrant cascada water source without "MonOilCu" treatment where <i>E. coli</i> and coliforms are present in high quantity. . . . .	53
4.13	Images of the membrane filtration results from the hydrant cascada water source with "MonOilCu" treatment where <i>E. coli</i> and coliforms diminished. . . . .	54
4.14	Schematic representation of antimicrobial action of "MonOilCu" against <i>E. coli</i> bacteria adapted from [144]. . . . .	55
4.15	The UV-Vis diffuse reflectance spectra of "MonOilCu" silica monoliths used in three different tests (a, b, c) in microbiological test. . . . .	56
B.1	Parameters used in the simulation for copper adsorption on silica surface. . . . .	61
B.2	Parameters used in the simulation for copper adsorption at position A on pure silica chabazite surface. . . . .	62
B.3	Parameters used in the simulation for copper adsorption at position B on pure silica chabazite surface. . . . .	63
B.4	Parameters used in the simulation for copper adsorption at position C on pure silica chabazite surface. . . . .	64





# List of Tables

1.1	Quality criteria of water sources for human and domestic consumption limits adapted from [95]. . . . .	22
1.2	Minimum number of samples to be taken according to the population served for the analysis of fecal coliforms in the drinking water distribution system adapted from [96]. . . . .	23
3.1	The most relevant monolithic samples with their synthesis parameters.	29
4.1	Listing of bond-length for copper adsorbed and close atoms of pure silica chabazite interface. . . . .	52
4.2	Initial parameters measurements of three samples of water (HWCS) and results of the microbiological test. . . . .	53
4.3	Parameters measurements after 72 hours treated with "MonOilCu" of three samples of water (HCWS) and results of the microbiological test.	54
A.1	XRD peaks data of silica monolith "MonOilCu" for calculation of the average crystalline size of $CuO$ nanoparticles. . . . .	59



# Chapter 1

## Background

### 1.1 Porous Materials

A porous material is any solid containing void spaces, it means the structure of the solid has spaces not occupied by the main framework of atoms [1, 2]. The International Union of Pure and Applied Chemistry classifies the porosity of materials as microporous (<2 nm), mesoporous (between 2 and 50 nm), and macroporous (>50 nm). The properties of porous materials depend on the chemical composition, atom arrangements, and largely on the pore morphology, size, and distribution [1]. Porous materials encompass a wide range of organic, hybrid organic-inorganic, and inorganic porous materials. The ones based on carbon like activated charcoal occupy the most famous place for its porosity, high surface area, and inexpensive cost [1].

Some examples of inorganic porous materials are the zeolites, which are very important in the industrial field and are built from corner-sharing  $MO_4$  tetrahedrals. The metal M represents silicon and aluminum atoms, and that is why they are also known as aluminosilicates. One precise aluminosilicate, as an example, is the chabazite, which can also exist as pure silica chabazite, which can be compared with porous silica materials except for the crystalline arrangement that it possesses [3].

Chabazite has cation-exchange properties because the aluminum replaces some silicon atoms and gives a negative charge in the structural framework, which is useful in water softeners [4]. Another porous material relevant in the adsorption and separation fields is the silica monoliths, which can be obtained as a powder or as a monolith. More recently, other porous materials have been discovered such as metal-organic frameworks (MOFs), porous organic polymers (POPs), and covalent organic frameworks (COFs), which have highly porous, contain remarkable high surface areas, and can be chemically functionalized [2]. Furthermore, they are highly desirable for chemical separation and immobilized catalysis.

## 1.1.1 Characteristics and properties of porous materials

### Zeolites

All zeolites are composed of an elementary structure of an aluminosilicate framework, which comprises a tetrahedral arrangement of silicon ( $Si^{4+}$ ) and aluminum ( $Al^{3+}$ ) cations that are surrounded by four oxygen ( $O^{2-}$ ) anions. A zeolite is composed of micropores and synthesized by a sol-gel process using organic and cationic templates [5]. More than 200 framework types have been discovered in the last century. Owing to a vast number of zeolites, the Structure Commission of the International Zeolite Association has designed a structure type code with three letters. A simple example is Analcime with *ANA* structure type code, and in Figure 1.1 one can visualize its characteristic porous structure. These pores, which are infinitely extended in one dimension and large enough to allow the diffusion of guest species (i.e., larger than six-rings), are also called channels [6]. Framework types can contain one-, two-, or three-dimensional channels. An essential characteristic of zeolites is the effective width of the channels, which determines its accessibility to guest species. The effective width is limited by the smallest free aperture along the channel. Thanks to their singular porosity and electrical properties, zeolites have an important participation in the industries as absorbents, molecular sieves, heterogeneous catalysts, etc. [1].

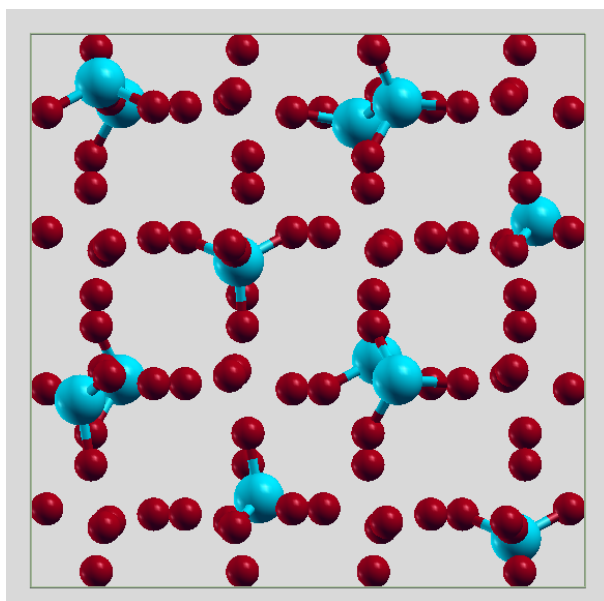


FIGURE 1.1: Illustration of crystalline porous structure of unit cell of Analcime zeolite performed with XCrySDen® (O: red, Si: light blue)

### Silica pure chabazite

Chabazite is a type of zeolite, and *CHA* is the structure type code. Chabazite is a three-dimensional small pore zeolite with pore openings of  $3.8 \times 3.8 \text{ \AA}$  and large ellipsoidal cavities of  $8.35 \text{ \AA}$ . Moreover, the chabazite framework contains secondary building units (SBUs) called double six-member rings taking account the silicon atoms without oxygen atoms [6, 7]. Nowadays, new species of chabazite have been found and synthesized since the first discovery of this mineral. For example, pure  $\text{SiO}_2$  chabazite has a chemical formula  $[\text{Si}_{36}\text{O}_{70.5}(\text{OH})_{2.9}]$  was synthesized by hydrothermal method and calcined [3]. The pure silica chabazite has been studied because of its potential applications on adsorption and separation of organic molecules as well as a catalyst in the conversion from methanol to ethylene. In Figure 1.2 is illustrated a crystalline structure of pure silica chabazite, which has a double six member-rings.

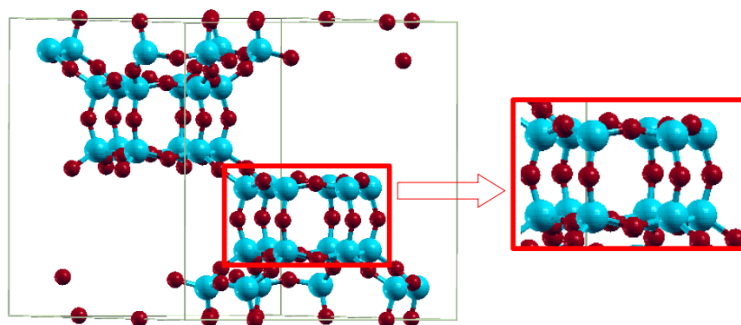


FIGURE 1.2: Illustration of crystalline structure of chabazite and double six member-rings made with xCrysDen® (O: red, Si: light blue).

### 1.1.2 Mechanism of synthesis of zeolites and pure silica chabazite

#### Zeolites

The majority of the zeolites are found naturally as a mineral inside cavities of volcanic lava diagenetic rock water reactions. However, zeolites are also produced in a synthetic way for industrial applications and to understand their chemistry [5]. The crystalline phase formation is a complicated process in zeolite synthesis, and different synthesis methods can be used depending on their use. One method is hydrothermal synthesis, which refers to the formation of materials in an aqueous solvent [6]. In brief terms, this method involves a mixture of amorphous reactants (silica and alumina) with a cation source at a basic medium. This reaction mixture

is heated in a sealed autoclave above 100 °C. After the above *induction period*, a crystalline zeolite product can be detected, which is recovered by filtration, washing, and drying. Essentially, all the amorphous material is replaced by an approximately equal mass of zeolite crystals (Fig. 1.3) [8].



FIGURE 1.3: Hydrothermal zeolite synthesis. The starting materials are converted by an aqueous mineralising medium ( $\text{OH}^-$  and/or  $\text{F}^-$ ) into the crystalline product whose microporosity is defined by the crystal structure [8].

On the other hand, Green Chemistry is one of the most outstanding science because the majority of methods have a great impact on the environment. In that spirit, a growing effort was devoted to green synthesis of well-known zeolites. So, the selection of the initial reactants of aluminum and silica is made from natural sources such as kaolin and rice husk, respectively [9]. As well as, some attempts to reduce organic or fabricate sustainable templates have been developed. First, a technology for recycling organic templates from zeolite microporous [10]. Second, the synthesis of zeolite materials using low toxicity or biodegradable templates as starch, fiber, gelatin, and the synthesis free of organic templates [11]. Third, synthesis routes that do not use organic templates called the template-free synthesis method have also been developed [12]. On the other hand, water and hydroxides are employed instead of the solvents and mineralizers, respectively [13].

### Pure silica chabazite

The synthesis of chabazite follows the general process used in the majority of zeolites, but some parts of the general procedure have been changed to take advantage

of the different properties that one can achieve. For example, for the cesium adsorption, a material was synthesized in the absence of organic-structure-directing agents and a seed crystal [14]. Furthermore, it was used as a mineralizer  $NH_4F$  powder. The synthesis of microporous  $SiO_2$  polymorphs involves a two-step process: the synthesis of a host-guest compound in the presence of a suitable Structure-Directing Agent (SDA), and its calcination to remove the guest organics [15]. The synthesis of the *CHA* zeolite under Organic SDA-free synthesis conditions has also been attempted with low micropore volume, where the yields obtained are below 50% [7]. The reaction mixture is heated in a sealed autoclave at 150 °C under rotation for four days in a convection oven. In Figure 1.4 is illustrated a representation of synthesis for pure silica chabazite.

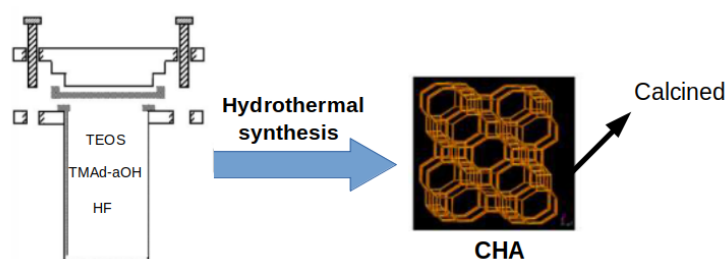


FIGURE 1.4: Hydrothermal pure silica chabazite synthesis based on the work by Dang [16].

Aforementioned, synthetic zeolites are fundamental in the industrial field because they can offer better mass transfer, low pressure, thermal stability, and good mechanical strength [17].

## 1.2 Monolithic porous materials

The term *monolith* means a single stone that has a common use for large rocks. In separation science, a monolith is defined as a continuous porous object whose morphology and pore structure can vary in a wide range [18]. In the middle of the twentieth century, the first monolith synthesis developed for researchers of Corning Corporation had poor control of the porosity. This process was called the Vycor® process, and was efficient for fabricating small monoliths but shows its limit concerning thick and bulky pieces. In fact, this process resulted in cracked and fractured monoliths due to the stress [19]. The search for novel and efficient materials as adsorbents to allow fast separations had major attention in packed columns



with smaller particles, but Professor N. Soga and K. Nakanishi were pioneers to develop continuous beds based on silica monoliths in 1991. They introduced this concept to the High-Performance Liquid Chromatography (HPLC). Consequently, the monolith advantages with well-defined macro and mesoporous for HPLC separation medium were published in 1993 by Tanaka et al. [19].

The porosity is the main characteristic of the monoliths because it is possible to obtain many pore sizes in a single monolith through each different mechanism of synthesis. The pores range from millimeter size down (macropores) to mesopores and micropores. Monoliths can have a broad monomodal distribution, a distinct bimodal distribution, and even a trimodal distribution with a hierarchical order of the pores [18].

Figure 1.5 shows silica monoliths composed of a single porous piece and exhibit two types of pores: flow-through pores in the micrometer ( $\mu\text{m}$ ) size range and mesopores in the nanometer ( $\text{nm}$ ) size range [20]. The micrometer-sized pores of the skeleton and the rapid mass transfer of the molecules in the diffusional mesopores being embedded in the skeleton of the monoliths give high accessibility through its stationary surface. The control of the pore structural parameters allows to obtain flow-through macro- ( $0.5 \mu\text{m}$  to  $6 \mu\text{m}$ ) and meso- pores ( $10$  to  $30 \text{ nm}$ ).

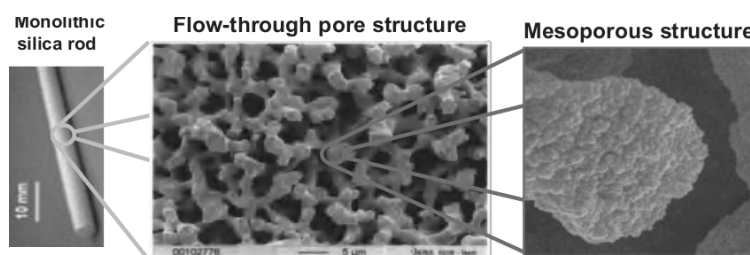


FIGURE 1.5: The structure of a rod monolithic silica with the bimodal pore structure: flow-through macropore structure, and mesopore structure in the silica skeleton [20].

Monoliths have a wide variety of types, such as a foam, a ceramic piece, and it can be made of a cross-linked polymer or composed of an oxide or even carbon. In this work, monoliths classification has been arranged according to the morphology, the porosity, and the characteristics that they have. The morphology can change between a thin disk, a membrane, a cylindrical rod, tubes, and a ceramic carrier of substantial size.

### 1.2.1 Monolithic disks

The structure of disk monoliths consists of interconnected microspheres (globules) that are aggregated in larger clusters. To develop this type of silica monoliths were useful basic concepts in macroporous polymers synthesis and separation of large molecules in the gradient mode. The first rigid disks had a diameter of 20 *mm* and a thickness of 1 or 2 *mm*, and the main features are the very low-pressure drop across the disk and the very high loading capacity [21]. The disk structure also enables high permeability, high capacity, and high-resolution power on a small scale in HPLC experiments (Fig. 1.6).



FIGURE 1.6: Image of disk monolithic silica used in HPLC columns [21].

#### Mechanism of synthesis

The need of developing disk monoliths arises from the requirement for separating large molecules, as proteins in the gradient elution mode. Indeed, this motivated the work of Belenkii et al. in the 80s that knew that separation of large molecules is more efficient through shorter path [22]. The preparation of the monolithic disks with a well-controlled internal structure regulates the variables on the polymerization, the mold, and environmental conditions. There are three main steps for the fabrication of monolithic disks: polymerization in the format of membranes or rods, cutting disks, and chemical modification. For the first step, a free radical copolymerization of a reactive monomer with a cross-linking monomer in the presence of a pore-forming solvent and an initiator. However, high-pressure drops could destroy the column due to the very low permeability and a pore size smaller than 10 *nm* [22]. On the other hand, a common limitation in this fabrication approach is the diameter of the mold, which directly affects the temperature of the polymerization and the morphology of the monolith.

## Applications

The thin disk monoliths of silica have been used in ion-exchange chromatography for the separation of proteins, which was called High-Performance Membrane Chromatography. Thus, monolithic silica disks are used as stationary phases in liquid and gas chromatography, capillary electrochromatography, and as support for bio-conversion and solid-phase synthesis [22–25].

### 1.2.2 Rod monoliths

The development of silica monoliths has been constant for columns in the High-Performance Liquid and Gas Chromatography because of their column efficiency, permeability, and separation time combined. That is why silica monoliths are preferred among porous particles columns of silica [26]. Moreover, it provided a higher efficiency per unit pressure drop, and the high permeability allowed the operation of a long column system. Different sizes of silica rod columns can be obtained by different synthesis methods (fig 1.7).

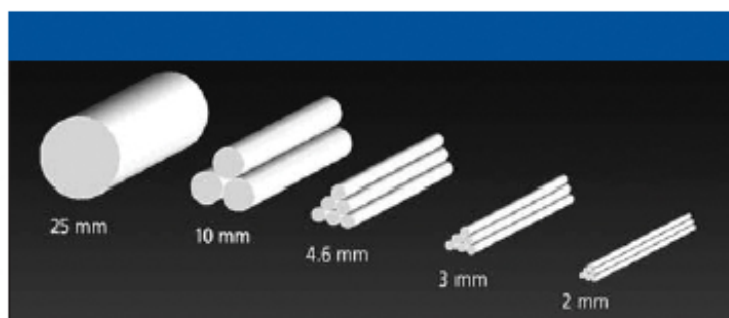


FIGURE 1.7: Image of the silica rod columns with different sizes [27].

### Mechanism of synthesis

One of the first synthesized rigid materials for their simple molding process was the monolithic porous polymer rods. The mold used by the synthesis is a tube and sealed in both ends [28]. In the process of synthesis, polymerization is a crucial step to obtain the desired monolith. Therefore, free radical polymerization is used in the molding process for fabricating cylindrical and rod monoliths with a homogeneous porous structure in capillaries and sealed tubes. Besides, the monoliths are readily achieved in a single polymerization step by heating bath or UV irradiation. Additionally, thermally initiated polymerization is another technique in which the kinetics of the process has reasonable control of different pore sizes in macroporous

materials [29]. The variation of the temperature induces changes in the nucleation rates and in the obtained pore distribution.

Photopolymerization is another technique that uses porogenic solvents for the preparation of large porous polymer monoliths. The suitable porogenic solvents for this method are mixtures that have low boiling points because the photopolymerization is carried out at room temperature. When polymerization is done, the next step is to remove the seals of the tube and connect it to a pump. The porogens and other soluble compounds that might remain in the porosity are removed while a solvent is pumped through the monolith. As a result, a very broad range of pore sizes in monoliths can be obtained using this method [28]. The benefits of this technique are the fast and simple “one-pot” preparation [30].

### Applications

The structure and the geometry of the pores in the monolithic columns have a fundamental role in chromatography experiments because they reduce run times through high flow rates while keeping adequate separation [31]. Aforementioned, the rod silica is demanded by its efficiency in separation, adsorption, catalysis, ion exchange, etc. Thus, rod monoliths are used in liquid and solid chromatography, and some examples are high throughput analysis of drugs and metabolites, separation of environmentally relevant substances, separation of food additives, separation of enantiomers, and separation of complex biological samples [32, 33]. As seen in these explanations, there is a direct relation between the specific shape of the macromaterial obtained through a design and its application. However, these monoliths do not only benefit from the shape.

## 1.3 Hierarchical porous materials

*Hierarchy* has a historical meaning from the Greek word related to the organization principle of nature [34]. In the context of porous materials, this term should be interpreted as systems possessing different pores types of bi-or multimodal pore size distributions independently of how the systems are interconnected [35]. Also, porous structures materials can be synthesized at multiple column length scales to obtain multiple functionalities [36]. In general, hierarchical porous materials contain porous structure consisting of multiple levels of porosities on different length scales from micro-, meso- to macropores, high surface area, large accessible pathways, low density, variable chemical compositions, and interconnected hierarchical porosity at different length scales [35, 37]. Consequently, these amazing properties give rise

to different possibilities of applications such as light-harvesting, electron and ion transport, high mass loading and diffusion, catalysis, photocatalysis, adsorption, separation, gas sensing, and biomedicine [38].

### 1.3.1 Types of hierarchical porous materials

A wide variety of hierarchically porous structures is found in the living organisms because this morphology is of key importance to achieve optimal properties in order to adapt to environmental changes in the long term constantly. Some examples of the natural occurring biological structures are diatoms, butterflies, wood, leaf, macaw feather, grass stems, kelp, coral, cotton, human bones, cuttlefish bones, and sponges (Fig. 1.8).

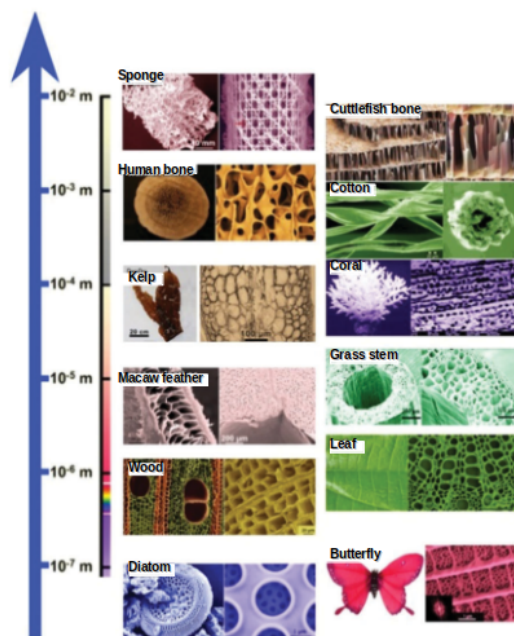


FIGURE 1.8: Illustration of hierarchical structured porous natural materials, placed alongside the length scale according to their critical dimensions. The Scanning Electron Microscopy or Optical Microscopy images of original biological hierarchically porous structures are shown above [39].

Apart from biological ones, inorganic hierarchically porous structures such as zeolites, titanium oxide, monoliths, spheres, and foams can be found [39]. For example, hierarchical material based on titanium oxide  $TiO_2$  has a synthesis process that controls nanoscale pore size and macroporous structure, which shows a good efficiency compared with other no hierarchical materials in dye-sensitized solar cells [40]. Also,  $TiO_2$  spheres have been synthesized using electrostatic spray technique

and show higher efficiency than other types of  $TiO_2$  [41]. Zeolites also have an excellent hierarchical pore structure where different nanoparticle types can be grafted in their mesoporous structure. High efficiency on photocatalytic hydrogen production is obtained when it is grafted  $Pt/CdS$  nanoparticles [42]. Therefore, the different types of hierarchically porous are very important to increase the efficiency of many applications, and porous silica materials will be explained in detail in the next section.

### 1.3.2 Mechanism of synthesis

Numerous approaches for the synthesis of hierarchically porous materials have been explored in the last years. One of the most developed has been the templating method, which has various types such as hard, soft, sacrificial templating method. First, hard templating, also known as "nanocasting", involves the utilization of porous or nonporous material to serve as a meso- or macroporogen for the formation of the hierarchical porosity. The procedure consists of the synthesis mixture, the addition of the solid template, crystallization of the precursors, and the post-synthetic removal of the solid template through calcination or dissolution in acids. Hard templates are carbonaceous materials, biological materials polymer spheres, mesoporous silica spheres. [34, 43].

Hard templates have some advantages, such as controlling the properties of the porous, chemically inert in the synthesis, and overcoming the need to control hydrolysis and condensation of guest species, which is obtained after the removal of the template, and their interactions with surfactants. However, this method is limited when using a multistep procedure. The procedure is more laborious and time-consuming, relatively high cost, and health hazards on the templates used [44]. In Figure 1.9 a facile hard-templating method scheme for generating tubular porosities is shown.

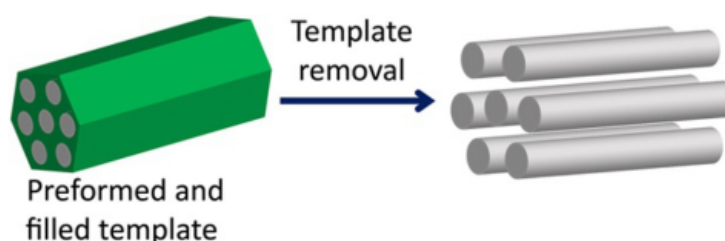


FIGURE 1.9: Hard-templating method scheme resulting from the addition of precursors to preformed templates and subsequent template removal [44]

One of the most versatile methods for the synthesis of hierarchically porous materials is the soft templating method. The soft templates include micelles, reverse micelles, micro-emulsions, block copolymers, surfactants, biomacromolecules, organic-based molecules, vesicles, etc. [45]. One of the advantages is to synthesize hierarchical porous materials with various morphologies under relatively mild conditions.

This method can be subdivided into primary and secondary methods as shown in Figure 1.10. In primary methods, all components are added at the beginning of one-step synthesis. Secondary methods are known by a two-step procedure, where all components except the surfactant are added in the first step, while the surfactant is added in the last step prior to the hydrothermal synthesis [34, 46].

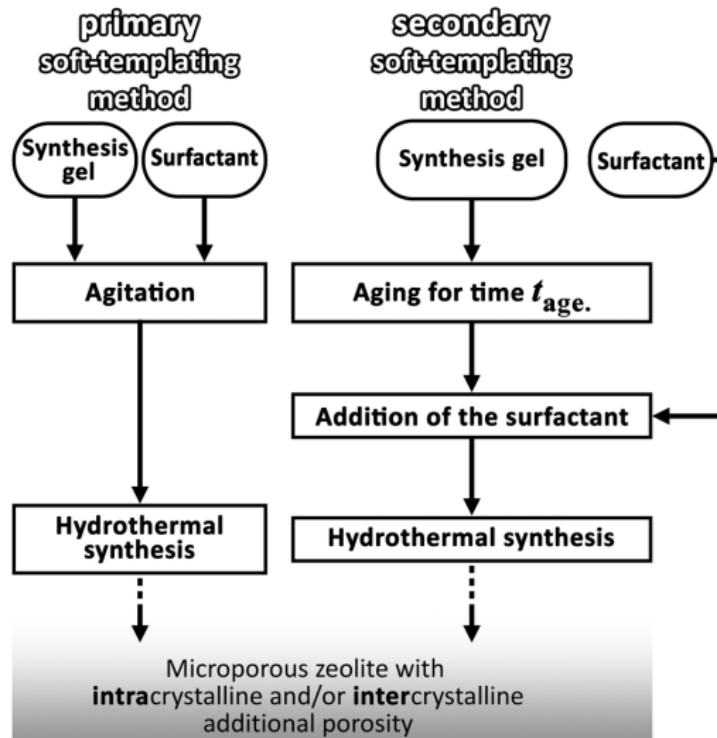


FIGURE 1.10: Methodology of the primary (left) and secondary (right) soft templating methods [34].

Moreover, multiple templating methods are also carried out to obtain hierarchical porous materials, such as the use of colloidal crystal (hard template) and surfactants (soft templates). This method starts with the infiltration of colloidal crystals with surfactant containing precursor, and then inorganic precursors condensed and crystallized. The removal of dual template involves the calcination at high temperatures or solvent extraction, which leads to the formation of bimodal pore distribution (meso and macro) [47]. Biomaterial hard templates and soft templates are

a good choice for multiple templating methods because the majority of biological materials are inexpensive [48]. Furthermore, a wide variety of templates, that can be used to synthesize several pore morphologies, are available. These biomaterials include animal bones, insect wings, plant leaves, etc. Macroporous polymer membranes, inorganic salts, ice crystals, and soft templates can be used as templates for the synthesis of bicontinuous macroporous inorganic oxide materials with controlled geometry [49]. The infiltration of the inorganic source or surfactant solution inside the porous structure of the membranes and the removal of the template are necessary to obtain the desired morphology.

Finally, the multiple template method for the fabrication of materials with a porous range from nanometer to micrometer uses the emulsion templates coupled with soft templates. The ways to make porous structures are using polymerizable surfactants, and the other is using gelation or freezing of microemulsion droplets. Another useful tool to have better control of the size pore is the combination of deformable and size-tunable emulsion drops with micelle templating. Consequently, emulsion templates and micelles or surfactants provide macro- and mesoporous structures, respectively [37].

### 1.3.3 Applications

Hierarchically structured porous materials are broadly used for catalysis, adsorption and separation processes, storage energy, and biomedicine. They present high surface areas for reaction, large dispersion of active sites at multi-modal pores, shortened mass diffusion paths or minimized diffusion barriers, more accessible for guest objects, and enhanced mass transport [37, 39]. Catalytic active sites for guest molecules are due to the micro-mesoporosity into a macroporous solid, which provide accurate size and shape selectivities for the reactants. These materials are used in acid catalysis, oxidation catalysis, and photocatalysis owing to their high accessibility of bulky molecules and their high diffusion rate of reactants and products [50, 51]. Some important properties such as high contact surface area, high storage volume, shape selectivity, control in the porous at different scales led to high adsorption capacities. During the last years, hierarchical porous materials based on silica have been used in separation and adsorption experiments. Hierarchical  $\text{CeO}_2$  spheres and nanocrystal microspheres are used for adsorption of dyes and remove toxic ions, respectively [52]. The high surface area and short diffusion length are important for energy conversion and storage applications. The advantages are efficient light-harvesting, especially in bio-materials replica or biocomposites, fast charge separation, and high current density, high gas permeability, high storage density,



fast electron and ion transport [35]. The multimodal porosity and high surface areas provide properties in biological processes such as bone tissue engineering, enzyme immobilization, and drug delivery. The biocompatibility and promoting cell adhesion, activity, excellent mechanical properties, controlled shape, and clinical use are some features of the hierarchical porous [35].

## 1.4 Emulsions as soft templates

An emulsion can be defined as a dispersed system in which the phases are immiscible or partially miscible liquids. The internal or dispersed phase, which can be oil or water, appears in the form of droplets, and the suspended phase (oil/water) is called the external or continuous phase [53]. The emulsion is stabilized by emulsifiers, which coat droplets to prevent them from coalescing within an emulsion. A common emulsion stabilizer is a surfactant, which is an amphiphile molecule where one part is hydrophilic (the “headgroup”), and the other is hydrophobic usually a long hydrocarbon, fluorocarbon, or siloxane chain [54]. Surfactants can be classified according to their head polarity because hydrophobic tails are often similar. A non-ionic surfactant has the head group no charge, an anionic or cationic surfactant is called when the head group has a negative or positive charge. Also, a zwitterionic surfactant is when the head contains both positive and negative groups [53]. In Figure 1.11 is shown an illustration of the formation and stabilization of an emulsion.

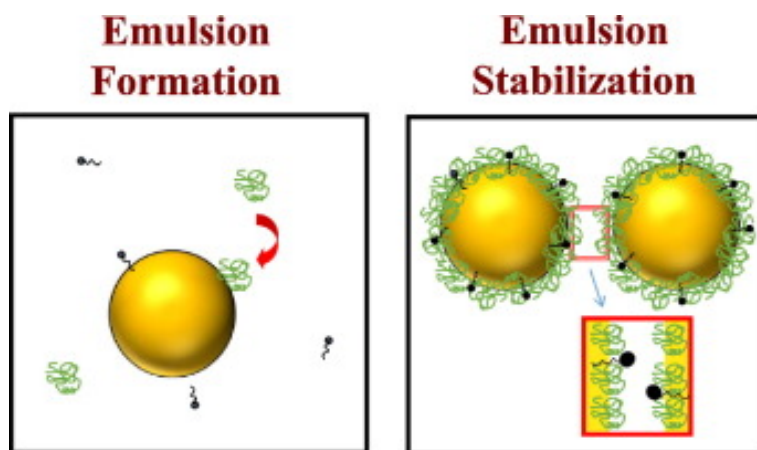


FIGURE 1.11: Illustration of the emulsion formation and stabilization [55].

### 1.4.1 Types of emulsions

The emulsion types are categorized into three classes such as water in oil (w/o), oil in water (o/w), and multiplied or complex emulsions. Water-in-oil emulsions comprise water droplets in an oil-continuous phase, and oil-in-water emulsions are attributed to droplets of the oil phase in a continuous flow of water. Multiple emulsion type is more complicated and is made of tiny droplets in larger droplets, which are suspended in a continuous phase [56].

Aforementioned, the common methods for hierarchical porous is templating and polymerization. The emulsion templating generally occurs within w/o emulsions, while emulsion polymerization and microencapsulation typically take place within o/w emulsions. The reactions in emulsion templating commonly occur within the external phase, while the reactions in emulsion polymerization occur in monomers solubilized within surfactant micelles. The original target for the emulsion templating was to synthesize hydrophobic cross-linked porous polymer monoliths with high internal phase emulsion polyHIPEs [57]. According to the phase internal volume of the materials, they can be classified as 1) high internal phase emulsions (HIPE) having internal phase contents  $> 74\%$ . 2) medium internal phase emulsion (MIPE) are with volume fractions of  $30 - 74\%$  of the phase internal phase. And 3) low internal phase emulsion (LIPE) with internal phase volume fractions  $< 30\%$ .

### 1.4.2 High Internal Phase Emulsions

High Internal Phase Emulsions (HIPE) can be defined as an internal (droplet) phase volume ratio of greater than  $74\%$ , which represent the maximum volume that can be occupied when uniform spheres are packed into a given space. This provides the most efficient packing arrangement [58]. HIPEs are used to prepare porous monolithic polymers known as polyHIPEs, titanium oxides, silica monoliths, etc. [59–61]. The porosity of these materials is due to a very high degree of interconnection between cavities throughout the matrix. Like ordinary dilute emulsions, HIPEs can be obtained in either normal (oil-in-water, o/w) or inverse (water-in-oil, w/o) forms. The HIPEs major phase is dispersed within the minor phase, as these types of emulsions are thermodynamically unstable, the phase separation and phase inversion occur very often during the preparation [57].

Besides, this fact has motivated researches to improve emulsion stabilization. HIPE stabilizers are used to keep good stability in polyHIPEs synthesis, the most common are poloxamers, but there are others like amphiphilic particles, gels, cellulose nanocrystals, gelatin particles, etc. [62, 63]. In recent years, many novel HIPE systems have been developed, including o/w, supercritical  $\text{CO}_2$ -in-water, and

nonaqueous emulsions such as oil-in-oil (o/o), ionic liquid-in-oil, and oil-in-deep-eutectic solvent [57]. For instance, a low-density, macroporous polyHIPE is usually produced by formulating a stable HIPE with a polymerizable continuous phase, polymerizing the continuous phase to “lock-in” the emulsion microstructure, and removing both the dispersed phase and the unreacted components of the continuous phase.

## 1.5 Poloxamers, an interesting surfactant with tunable properties

HIPE stabilization is an important part of the synthesis of hierarchical porous monoliths because it can prevent separation and inversion of the phases. Surfactants are the most used ones due to efficient stabilization strategies in different types of emulsions. Due to the lower surface tension between two liquids, liquid-gas, and liquid-solid give to the surfactant properties such as detergents, wetting agents, and emulsifiers agents [53].

The commercial names for these surfactants are poloxamers or Pluronic® manufactured by ICI and BASF, respectively [64]. Pluronic® is a synthetic amphiphilic triblock copolymer composed of a central hydrophobic chain flanked by two hydrophilic chains [65]. For example, hydrophilic poly(ethylene oxide) (PEO) block and hydrophobic poly(propylene oxide) (PPO) are organized in the following way PEO-PPO-PEO [66]. Also, poly(ethylene glycol) (PEG) block, poly(propylene glycol) (PPG) arrangement as PEG-PPG-PEG [67]. The chemical structure of Pluronic® PEO-PPO-PEO is shown in Figure 1.12.

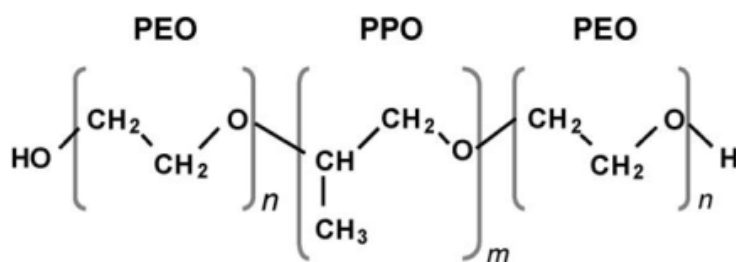


FIGURE 1.12: Illustration of the chemical structure of a poloxamer [68].

### 1.5.1 Types of poloxamers

A specific nomenclature for Pluronic® was introduced by BASF (original manufacturer) that consists of a letter indicating the morphism of each one (liquid (L), paste (P), and flake (F)). The first one or two digit(s) are associated to the molecular weight of the PO blocks in each molecule as shown in the vertical axis in Figure 1.13 [64, 69]. The last digit shows one-tenth of wt% of EO content in each molecule as shown in the horizontal axis in that Figure [70]. As an example, P104 and P84 are both pastes, having the same molar mass percentage of PEO per unimer (40%) with longer PO units for P104.

The physical and chemical properties of Pluronic® can be tuned easily by modification of the molar mass ratio between PPO and PEO block. Due to those modifications, pluronic block copolymers offer more than 50 amphiphilic, water-soluble, and polymorphic materials (Fig. 1.13) [69].

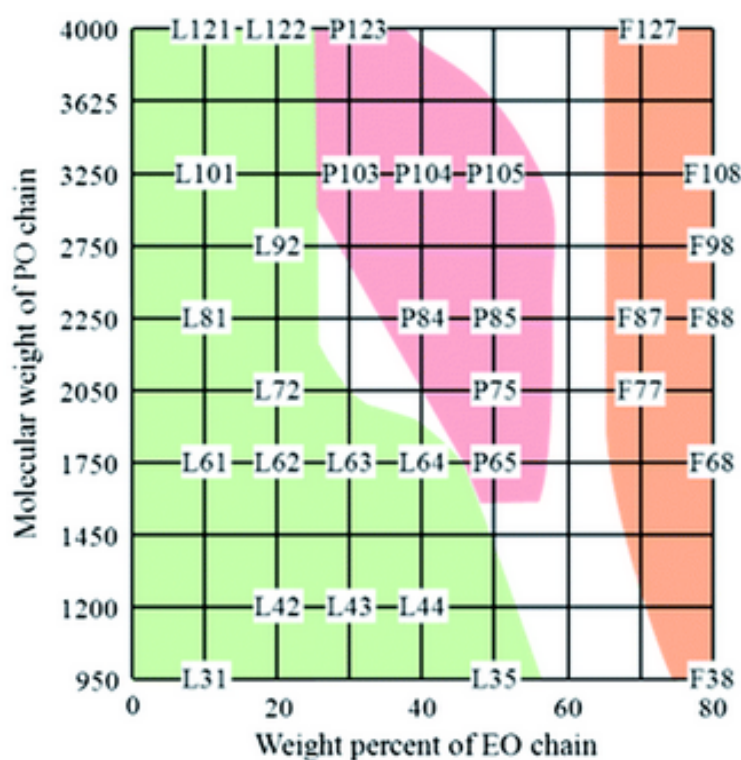


FIGURE 1.13: Pluronic® grid (colour code: physical state of copolymers under ambient conditions: green = liquid; red = paste; orange = flake) [69].

## 1.5.2 Applications of poloxamers

There is a wide range of uses of poloxamers owing to their synthetic versatility and tunability. The surface properties can support drug delivery and possible intrinsic biological activity, which are desirable for nanomedicine [71]. Then, Pluronic® have an important role in drug delivery systems, biological response modifiers, surfactants, gelation, template for mesoporous materials, among others [69, 72–74]. Poloxamers are the main tool to obtain hierarchical porous materials with HIPE, and the type utilized during the synthesis procedure depends on the kind of emulsion that is desired to achieve as oil in water (o/w), water in oil (w/o), or multiple ones. HIPEs (w/o) are usually achieved with sorbitan monooleate and polyglycol polyricinoleate (PGPR), while for HIPEs (o/w) the triblock copolymers based on poly(ethylene oxide) (PEO) and poly(propylene oxide) (PPO) are the most used like for example P123 [57].

## 1.5.3 Pluronic® P123

Pluronic® P123 is a copolymer commonly used as a surfactant. Surfactants are amphiphile molecules where one part is hydrophilic (the “headgroup”) and the other is hydrophobic, usually a long hydrocarbon, fluorocarbon, or siloxane chain [54]. Pluronic® P123 is symmetric triblock copolymer (EO<sub>20</sub>PO<sub>70</sub>EO<sub>20</sub>), which contains a hydrophobic polypropylene oxide block (PPO) surrounded by two hydrophilic polyethylene oxide blocks (EO) arrangement in an alternating linear fashion, PEO-PPO-PEO. These different amphiphilic polymers differ by their molecular weights and variations in the EO/PO ratio. Likewise, by changing the repeating units of the Pluronic®, it is feasible to modify the size, hydrophilicity, and hydrophobicity of the system. The particular nature of Pluronic® P123 allows it to form spherical, hexagonal, and tubular micelles, which will be used in this work. It is very important to remark that hierarchical silica monoliths can be synthesized by using both o/w HIPE and P123 poloxamer. This combination gives a very soft ambiance in the chemistry involved during the process. In this sense, P123 works as both emulsion stabilizer and mesoporous template, while the oil droplets are the templates that lead to the macroporosity obtained.

## 1.6 Applications of hierarchical silica monoliths

Hierarchical monolith applications are owing to their high accessibility and high storage capacity of the multiscale porous. Since the last decades, monolithic silica has been extensively used as a packing material of columns for high-performance

liquid chromatography [47]. Likewise, the combination of synthesis methods as the phase separation and sol-gel process gives a remarkable potential for catalysis, and adsorbents improved its efficiency and productivity [75]. Besides, hierarchical monoliths synthesized through 3D printing has been explored for solid-gas catalytic application [76]. The control of the pore characteristics at each length scale and the facility to do chemical functionalization allow significant application in tissue engineering as scaffolds for cell growth [77].

Moreover, it is significant to remark about the separation and functionalization of these materials because these properties allow to work in different applications in environmental science. As an example, the decontamination of cesium in water through the functionalization of silica monolith network [78]. Additionally, silica monoliths are easy to dispose of after to sorption of contaminants in their network. Many studies in hierarchical silica monoliths have confirmed the efficiency of their depolluting properties of water [79]; therefore, it is convenient to review information about control of water quality in Ecuador and their lackings.

## 1.7 Theoretical simulations as a tool to study porous materials

Nowadays, computational methods are recognized as an indispensable tool in science as chemical, physical, biomedical and engineering sciences. Moreover, these methods have been developed rapidly making predictions of physicochemical properties of chemical systems at the molecular level where in some cases, computational chemistry could replace experiments, and these are used to confirm predictions [80].

The information on the activity of the nanoporous materials at the molecular level has been a challenge in the last years because it is challenging to carry out experiments at this level. For example, to understand a reaction inside the pores of the zeolite requires much information about diffusion from the active site, adsorption on the active site, and desorption [81]. A wide range of computational studies of porous materials focusing on zeolites and metal organic frameworks (MOFs) because of the interest in understanding the processes involved and to optimize industrial applications [82, 83].

Computational chemistry methods use interatomic potentials called force fields to understand the behavior of the chemical system. A wide variety of methods of computational chemistry can be classified according to their accuracy and dimensions. These methods can be classified between quantum and classical methods,

which are using forcefield. The quantum methods, such as Density Functional Theory (DFT), show a greater accuracy but can only model a system of few hundred atoms, in contrast with classical method, which allows much bigger systems with lower accuracy. Therefore, researches in nanomaterials at the molecular level as quantum chemistry calculations based on DFT is an important tool to make simulations with a high accuracy level. Among the most used simulations codes, Quantum Espresso and VASP are two representative codes that use a plane-wave approach [84, 85]. The advantage of the plane-wave approach relies on the periodic nature of the waves, which are particularly well fitted for representing a material where a repetition of a unit-cell is used. However, the disadvantage is that plane-wave methods require a large number of basis functions (increasing significantly memory requirements), and local crystalline orbitals do not efficiently treat low symmetry systems [86].

There are several theoretical studies in the porous materials field for understanding the behavior of the interaction in the adsorption process at a quantum level due to their great importance in developing devices to achieve their maximum performance. For example, the prediction of adsorption of greenhouse gas (perfluorocarbon compound) uses porous materials such as activated carbon. Through Density Functional Theory (DFT) methods using appropriate and specific parameters for their calculations, the results show good agreement with experimental data for adsorption of perfluorocarbon [87]. Moreover, one can determine the effects on the correlation functional on the structural and electronic properties of porous material like  $TiO_2$  (Anatase) through theoretical studies. The results have a special interest because it helps to understand the molecular properties of the Anatase, which possesses high photoreactivity used in industrial catalysis [88]. One theoretical study that has motivated this work is the adsorption of water in the silica surface because it has a similar simulation goal. The electronic and binding properties studied between silica and water suggest the implementation of transport materials and sensing applications [89].

## 1.8 Drinking water

Water is the most important substance on Earth because it is necessary for living beings. There are two definitions of water: raw water and drinking water. Firstly, raw water is in the environment without treatment to modify their characteristics. Second, drinking water is defined when the chemical, physical, and microbiological properties of water have specific levels guaranteeing its suitability for human consumption. Furthermore, drinking water is used for individual or collective needs,

such as personal hygiene, cleaning items, materials, or utensils. In Ecuador, around 740 hydrographic units of water exist in the continental and island regions. The availability of superficial and groundwater is around 21.067 cubic meters per inhabitant per year [90]. The most effluent sources of water are coming from the Pacific Ocean and Amazon River.

In Ecuador, 7 of 10 people drink safe water (Free of *E. coli* bacteria) [91]. This data was obtained from the "Instituto Nacional de Estadísticas y Censos" (INEC) through testing water for *E. coli* bacteria in around ten thousand households in the urban, rural areas. However, the majority of the 30 percent without drinking water access are located in rural areas with low-income families. For example, the Galapagos Islands region has been a challenge to provide safe water because the majority of water is the brackish water. Brackish or briny water has more salinity than freshwater, but not as much as seawater.

Galapagos Islands consist of 3 main islands: Santa Cruz, San Cristóbal, Isabela, and other small islands not populated. The most populated island is Santa-Cruz, a new technology has been implemented in the last years to achieve the goal of providing safe drinking water to the citizens. Nevertheless, the possibility of proper treatment of brackish water is expensive, and the distribution of the treated water does not take into account communities far from the city. Nowadays, the efficient way to provide water is through water tank trucks that are not regulated by the decentralized autonomous government of the city. Some of these tank trucks provide water to the citizens from sources of the public enterprise, others from water sources with low quality as a hydrant called "La cascada". This clandestine hydrant is a groundwater source containing brackish water and is contaminated due to human activity such as sewage water of septic systems. In Figure 1.14 is shown the water cycle on the island and the contamination of groundwater sources [92].

Therefore, this water source contains microbiological contamination like *E. coli*, fecal coliforms, which can transmit diseases as diarrhea or skin irritation [93]. In this context, to decontaminate this source of water, it is necessary to know the regulation of water that exists in Ecuador.

### 1.8.1 Regulation of drinking water in Ecuador

In the past years, the government entity which regulates the quality of drinking water, sewage water and freshwater of any source was the "Secretaría Nacional del Agua" (SENAGUA), however, in May 2020 it has been merged with the "Ministerio del Ambiente" and the new government entity is called "Ministerio del Ambiente y Agua del Ecuador" [94]. This organism is in charge of regulating certain parameters



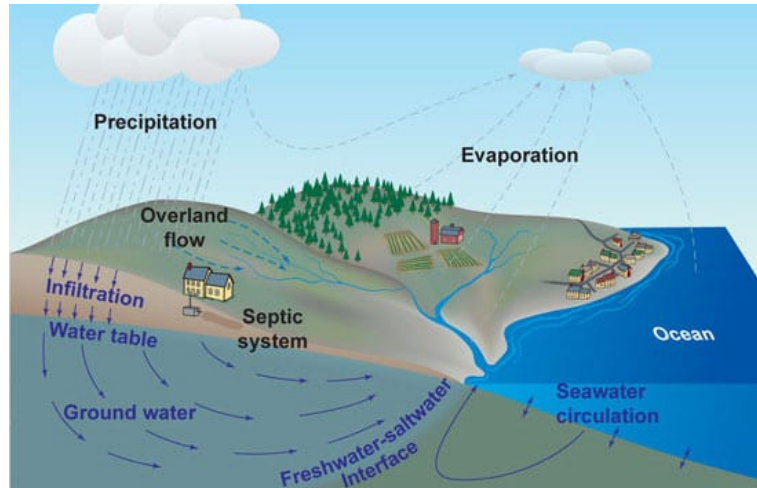


FIGURE 1.14: Water cycle in the island and the contamination of groundwater sources [92].

that drinking water, sewage water, and freshwater have to accomplish. These parameters are different from one to another type of water, and they are fixed under a scientific and technological criterion for human uses and consumption as well as for living beings protection [94].

For drinking water, the control is based following the rules of documents as NTE INEN 1108 (2014) and Anexo 1, which is based on the guidelines for drinking water quality by the World Health Organization [95]. In Table 1.1, one can see the most commonly analyzed parameters in the water quality laboratory for drinking water, and their corresponding allowed values.

TABLE 1.1: Quality criteria of water sources for human and domestic consumption limits adapted from [95].

Parameters	Symbols	Units	Maximum allowed limit
Oils and fats	Soluble substances in hexane	mg/L	30.0
Fecal coliforms	–	MPN or CFU /100 mL	1000
Escherichia coli	<i>E. coli</i>	–	Absence
Copper	Cu	mg/L	5.0
Aluminium	Al	mg/L	5.0
Free chloride	Cl	mg/L	0.3 to 1.5

Adapted from "Anexo 1 del libro VI del texto unificado de legislación secundaria del ministerio del ambiente".

The units for microbiological parameters are *CFU*: colony-forming units obtained through membrane filtration method, and *MPN*: most probably number obtained through multiply tubes method [95, 96]. The minimum number of microbiological tests are realized according to the population, which is benefited from the drinking water. That analysis is made in the drinking water distribution system and several points (houses, hospitals, schools, etc.) in the cities. In Table 1.2 shows the minimum frequency, which should accomplish each public entity of water of each city in Ecuador [96].

TABLE 1.2: Minimum number of samples to be taken according to the population served for the analysis of fecal coliforms in the drinking water distribution system adapted from [96].

<b>Population</b>	<b>Total number of samples per year</b>
<5000	12
5000-100000	12 per each 5000 persons
>100000-500000	120 and 12 more per 10000 persons
>500000	600 and 12 more per 100000 persons



## Chapter 2

# Problem Statement

Water is the most important resource for living beings on the planet, and the biggest reserves of freshwater are in Latin American countries. Paradoxically, these countries are the most affected by the lack of drinking water in rural areas, and Ecuador is not an exception. The biggest cities of Ecuador provide drinking water obtained through natural reserves of freshwater and treatment plants. Therefore, in the most remote rural areas, several families do not have access to drinking water provided for the government owing to the high cost involved in the equipment for treatment plants. Even though an increasing researching effort has been devoted to solve this problem of deficiency of drinking water, the current proposed materials still suffer from high production cost or instability. One of these methods is the use of functionalized bio-polymers which determines the bactericidal effect of copper. The majority of families use rainwater or groundwater without any kind of treatment for human consumption. Thus, low-cost alternative materials synthesized, with recycled materials and reagents, like copper functionalized hierarchical silica monoliths along with the intent to decontaminate water in an area with low water quality, such as Santa Cruz - Galapagos Islands, has motivated this research work.

## 2.1 Objectives

### 2.1.1 General Objective

Synthesis of hierarchical silica monoliths by high internal phase emulsion method using recycled cooking oil, and the evaluation of its antibacterial activity on groundwater samples from Galapagos Islands.

### 2.1.2 Specific Objectives

- To synthesize and characterize a monolith made through the well-established HIPE method.

- To verify the possibility of preparing a silica monolith using recycled cooking oil as an oleic phase.
- To determine the hierarchical morphology of synthesized silica monoliths by HIPE method through Scanning Electron Microscopy and Nano-Computed Tomography.
- To functionalize, in an in-situ manner, the silica monolith with copper as a possible model contaminant and doping agent.
- To verify the incorporation of copper inside silica monoliths and determine the position of copper through spectroscopic techniques.
- To study the interaction of copper with silica surface through quantum chemical methods using silicon surface and chabazite as a model of the internal porosity of the silica monolith.
- To test the copper-functionalized hierarchical silica monolith as a bactericidal agent for depollution of tap water samples originating from hydrant of Santa Cruz, Galapagos Island.

## Chapter 3

# Methodology

### 3.1 Synthesis of hierarchical porous silica monolith

In this work, silica monoliths from HIPE method were prepared based on the in-situ process reported in the reinforced silica monoliths functionalized with metal hexacyanoferrates for cesium decontamination: a combination of a one-pot procedure and skeleton calcination [97].

#### 3.1.1 Materials and reagents

The materials used for the synthesis of all monoliths are the following: hot plate magnetic stirrer, 100 mL and 50 mL beakers, magnetic stirrer, 1000  $\mu$ L - 100  $\mu$ L micropipette, tubular plastic mold, and glass desiccator. On the other hand, the reagents are: Tetraethyl orthosilicate (TEOS, 98%), Pluronic® P123 (EO<sub>20</sub>PO<sub>70</sub>EO<sub>20</sub>,  $M_n = 5800$ ), hydrochloric acid (HCl, 37%), sodium fluoride (NaF, 99%), copper (II) nitrate trihydrate ( $Cu(NO_3)_2 \cdot 3H_2O$ , 99%) from Sigma Aldrich and used as received. The organic solvent cyclohexane (99.9%) was purchased from Fischer Chemical. Also, the recycled cooking oil recovered from the experiments performed in the lab.

#### 3.1.2 Experimental procedure

In a 100 mL beaker over a stirring plate, 2 mL of P123 of an acidic solution (P123, 20 %w) was put with an initial stirring of 400 rpm. 1.075 mL of TEOS were added, slowly drop by drop into the beaker. The hydrolysis phenomenon of the TEOS with the acidic solution of P123 was carried out during 30 minutes. Silica precursor polymerization and pH regulation were enhanced adding 20  $\mu$ L of NaF (at 8 g/L). At this point, stirring velocity was increased at 500 rpm, and the emulsification process began with the addition of 5.1 mL of cyclohexane drop by drop. After 5 minutes,

a white emulsion appeared, and it was placed into a screw cap resin vial that conferred the form to the monolith. The sample was placed into a desiccator at room temperature during eight days and aging for eight days, more without a screw cap for allowing the slow evaporation of the cyclohexane (which forms macroporous). In the final step, the calcination of the samples was performed in a muffle furnace to free the mesoporosity by P123 elimination with a calcination ramp from room temperature to 500 °C, and a heating rate of 1 °C/min. A detailed scheme showing step by step the synthesis process can be find in Figure 3.1.

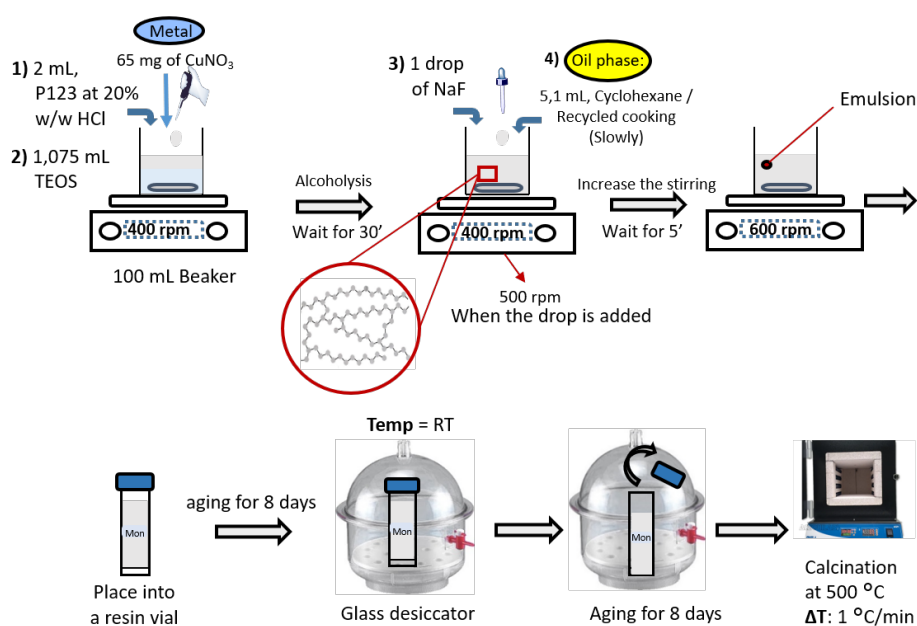


FIGURE 3.1: General scheme of the synthesis of silica monoliths.

For the synthesis of the other silica monoliths, the cyclohexane (phase oil) was changed by recycled cooking oil of the lab practices. The recycled cooking oil was pretreated by filtration in order to remove any solid particle in the oil. In the functionalization of the silica monoliths, the copper (II) nitrate trihydrated and Pluronic® P123 was added simultaneously. Moreover, cyclohexane (phase oil) and recycled cooking oil were used as the oil phase. The most relevant monoliths are detailed in Table 3.1. In this Table is detailed the synthesis parameters of hierarchical silica monoliths used for this work.

TABLE 3.1: The most relevant monolithic samples with their synthesis parameters.

Name	TEOS (mL)	Oil phase(mL)	Copper (mg)	Calcined
Mon1	1.075	Cyclohexane (5.1)	0	No
Mon2	1.075	Cyclohexane (5.1)	0	Yes
MonCu	1.075	Cyclohexane (5.1)	80	No
MonOil	1.075	Recycled cooking oil (5.1)	0	Yes
MonOilCu	1.075	Recycled cooking oil (5.1)	65.8	Yes

## 3.2 Characterization Techniques

The characterization of the obtained materials provides comprehensive information about the structure and properties which are useful for many applications. The techniques used for this work were X-ray Powder Diffraction (XRD), Attenuated Total Reflection FTIR, Diffuse Reflectance UV-Vis Spectroscopy (DRS-UV-Vis), Scanning Electron Microscopy (SEM), and X-ray Nano-Computed Tomography (Nano-CT).

### 3.2.1 Scanning Electron Microscopy

This is a characterization technique useful that can provide information on surface topography, crystal structure, crystal orientation, chemical composition, phase distribution, and electrical behavior of the top 1  $\mu\text{m}$  or so of specimen [98, 99]. The SEM magnification can typically reach 10 – 500000 times and provides a detailed field with gray-scale images. The sample to be analyzed must be conductive, otherwise, it is required a base on which the sample is placed, such as graphite or a thin metal layer like gold or aluminum, to provide the necessary conductive character.

The principle of the method is based on incident electrons beam from an electron gun (2 – 40  $eV$ ), which is impacted on the surface of the specimen, and the reflected (or back-scattered) beam of electrons is collected. Then, it is displayed at the same scanning rate on a cathode ray tube. Besides, there are three types of electron guns and the most common is the tungsten hairpin filament. The others are lanthanum hexaboride filaments and field emission guns. Usually, Energy Dispersive X-ray Spectroscopy (EDS) operates together with SEM to provide qualitative, and semi-quantitative information on the composition of the scanned specimens [100]. A scheme of the SEM structure is detailed in Figure 3.2. There are some relevant advantages of this equipment, such as the large specimens (200  $mm$ ) that can be scanned, non-destructive evaluation of the specimen, and less consuming time in the specimen preparation [98].



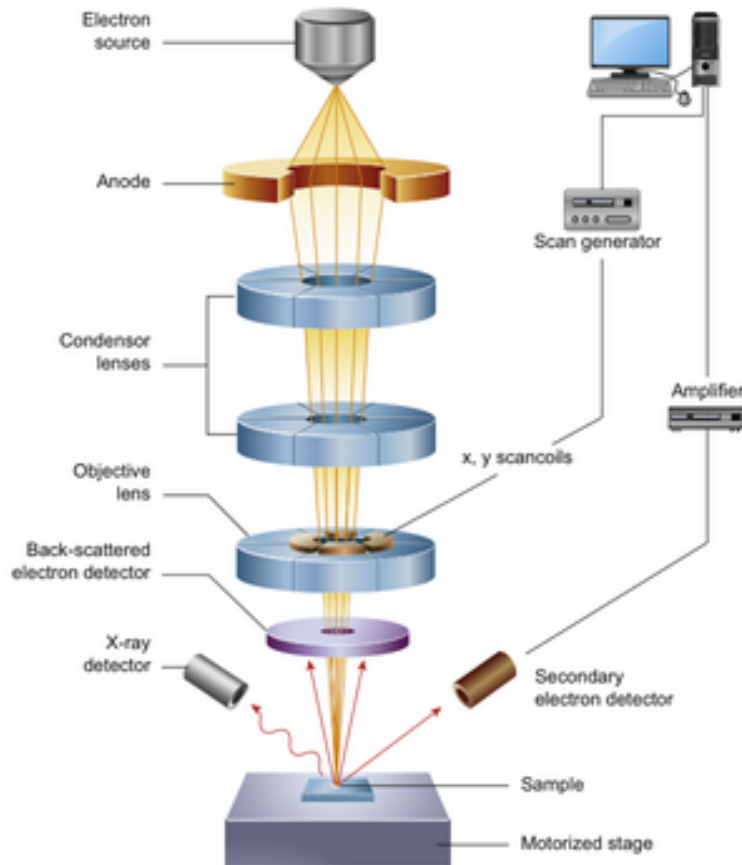


FIGURE 3.2: Schematic diagram of the core components of a SEM microscope [101].

In this work, SEM images were taken using a Thermo Scientific Phenom XL G2 Desktop SEM, where primary electron energy was 15 kV and a magnification of 2700x and 6900x.

### 3.2.2 X-ray Nano-Computed Tomography

X-ray Nano-Computed Tomography imaging is a non-destructive technique to characterize material microstructure in three dimensions at a micron level spatial resolution [102]. Specimen preparation is typically minimal. X-ray Nano-tomography has its roots in Computerized Axial Tomography (CAT or CT) scans that have been used for medical imaging for 40 years. The benefits of 3D maps of the internal structure allow the adaptation in fields like Materials Science [103]. The basic principles invoked for CT imaging are the X-ray absorption physics, which is relevant for the 2D projection images, and the tomographic reconstruction mathematics, which is invoked when producing a 3D volume from the series of 2D projection images [102].

At the most basic level, tomographic reconstruction of projection images provides us with a 3D map of X-ray absorption.

The structure of the micro and nano-CT system consists of an X-ray source, a stage or holder space for the object being imaged, and a camera or detector. As well, to analyze a wide variety of samples, micro and nano-CT has four kinds of scanner hardware configuration: pencil, fan, parallel, and cone-beam geometries. In Figure 3.3 is shown the principle of these geometries, where have differences in the type of X-ray source and the type of utilized detector. Moreover, beam collimation is used in the Pencil and Fan beam before reaching the object, and it helps for the narrow and direct beam.

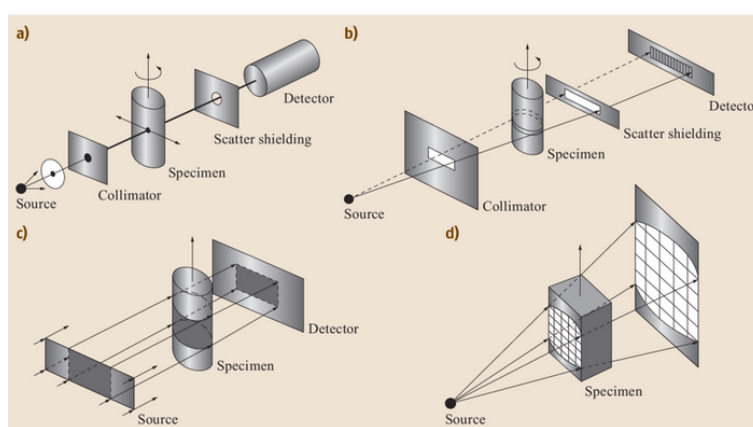


FIGURE 3.3: Illustrations of laboratory micro-CT scanner geometries: (a) Pencil beam. (b) Fan beam. (c) Parallel beam. (d) Cone beam [104].

With the aim to obtain a wide visualization of porosity of the calcined silica monoliths, the samples were analyzed in a SkyScan 2211 X-ray Nano-Computed Tomograph [105]. The characterization was carried out based on similar experiments with porous silica materials for 2D analysis. A small piece of a monolith (0.5 g) was placed in the sample holder of the equipment. X-ray beam worked between 20-25 kV, reconstructed pixel size: 3  $\mu\text{m}$ , computational time: 29 min 23 s, 1402 (2D) projection images are captured, and lower and higher gray threshold are 53 and 255, respectively.

### 3.2.3 X-Ray Powder Diffraction Spectroscopy

Another useful technique to verify the metal impregnation is X-Ray Powder Diffraction (XRD), which uses X-rays to investigate and quantify the crystalline nature of materials by measuring the diffraction of X-rays from the planes of atoms within

the material [106]. Some definitions are important to understand how the equipment works such as X-rays, which are electromagnetic radiation of very short wavelengths in the angstrom  $10^{-10}$  m and nanometer  $10^{-9}$  m region. X-rays are produced when a particle, which is electrically charged with sufficient kinetic energy, is rapidly decelerated. Bragg-Brentano geometry is the type geometry based on reflection geometry where the source and detector are on the same side of the sample and the most found in the laboratories. There are two types of Bragg-Brentano geometry which are  $\theta$ - $2\theta$  and  $\theta$ - $\theta$  [106, 107]. The essential characteristics of this geometry are the relationship between  $\theta$ - $2\theta$  that is maintained throughout the analysis, and the distance between the X-ray source and the sample. Also, the sample and the receiving slit-detector are fixed. An illustration of the Bragg-Brentano geometry is shown in Figure 3.4.

One of the important concepts of radiation is the Bremsstrahlung radiation or braking radiation that produces a continuous spectrum when electrons hit the target [107]. The process to generate X-rays involves the  $K\alpha$  lines, which are produced when an electron from one of the outer shells falling into the vacancy created in the K shell [106]. X-ray diffraction requires the use of monochromatic radiation, which are single wavelength X-rays. Thus, the high intensity and monochromatic nature of characteristic lines make them ideal for XRD analysis. For Cu radiation, the  $K\alpha$  X-ray is 90 times of the Bremsstrahlung X-Rays.

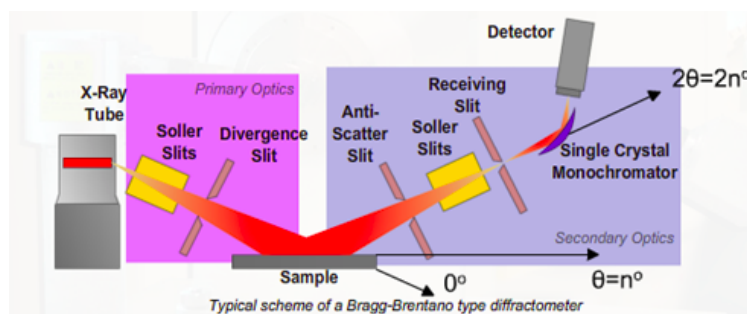


FIGURE 3.4: A Bragg-Brentano geometry based diffractometer [107].

For this work, some monolith samples pieces were crushed until a fine powder was obtained. Then, they were analyzed in a powder diffractometer Miniflex-600, Rigaku, with a D/tex Ultra2 detector. The X-ray generator was operated at 40 kV and 15 mA, in a sealed tube  $\text{CuK}\alpha$  radiation source. Additionally, for collecting data was employed a  $\theta/2\theta$  scan-axis, with a  $0.005^\circ$  step width in range from  $5^\circ$  to  $90^\circ$  ( $2\theta$ ), and the D/tex Ultra2 detector in 1D scan mode.

### 3.2.4 Attenuated Total Reflection FTIR Spectroscopy

Most of organic or inorganic compounds have covalent bonds which absorb electromagnetic radiation frequencies in the infrared region. The principle is focused on the vibrational range of the infrared region (IR) ( $4000\text{ cm}^{-1}$  -  $400\text{ cm}^{-1}$ ) where the molecules are excited to a higher energy state when absorbing infrared radiation [108]. Owing to every type of molecule that has a different natural frequency of vibration, the infrared spectrum can be used for molecules as analogous to fingerprints for humans. As each chemical group vibrates at a specific frequency, it can be used to get precious structural information about a molecule. There are two types of infrared spectrophotometers such as Disperse and Fourier transform (FT) instruments. Both provided identical spectra, however, FT infrared instrument provides a spectrum with greater sensitivity and speed than the Dispersion instrument [108]. The advantages of the FT-IR are due to a mathematical operation known as the Fourier transform that can separate the individual absorption frequencies from the general complex signal called interferogram, producing a spectrum virtually identical to that obtained with a dispersive spectrophotometer [109].

A common issue in the traditional FT-IR instrument is found in the sample preparation because it is messy and time-consuming. Both liquid and solid samples suffer from inevitable reproducibility issues given in the complexity of the sample preparation methods. The quality of measurements can be affected when fragile and hygroscopic materials are involved if handled or stored incorrectly. However, in recent years Attenuated Total Reflectance (ATR) has combating these challenges in the infrared analysis because it requires no sample preparation [110, 111]. ATR takes advantage of the property of total internal reflection, and it measures the changes that occur in the totally internally reflected infrared beam when the beam comes into contact with a sample [109]. An infrared beam is directed into a dense optical crystal (Diamond is the best for ATR) with a high refractive index at a certain angle and this creates an evanescent wave which extends beyond the surface of the crystal into the sample held in contact with the crystal (Fig. 3.5) [111]. All of these characteristics allow this equipment to have quick and good resolution measurements, and it has a wide range of applications in the scientific and industrial fields [112–114].

In this work, the IR spectrophotometry was performed with an Agilent FTIR, Cary 630 spectrophotometer equipped with a single reflection, diamond attenuated total reflectance (ATR). The scanning range for the obtained samples was from  $650\text{ cm}^{-1}$  to  $4000\text{ cm}^{-1}$ .

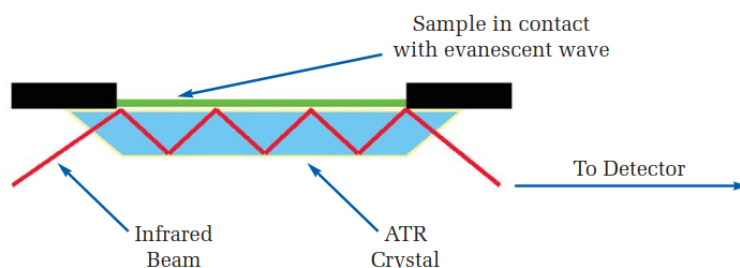


FIGURE 3.5: A multiple reflection ATR system [111].

### 3.2.5 Diffuse Reflectance UV-Vis Spectroscopy

Around 1940, the first diffuse studies were carried out in the visible region. Five decades later was expanded and exploded to the near-infrared and mid-infrared regions. The main applications were in the industries for quality control of products characterizing catalytic surfaces [115]. Nowadays, Diffuse Reflectance Spectroscopy (DRS) can be defined as an optical phenomenon used in UV-Visible, Near-Infrared (NIR), Mid-Infrared (DRIFT) regions to obtain molecular spectroscopic information of solid materials and fine powders.

The principle is that samples are irradiated with an electromagnetic beam source. A reflectance spectrum is obtained by collecting the signals and the analysis of the surface-reflected electromagnetic radiation as a function of frequency or wavelength. The reflected signals are a composition of two types of reflections that can occur: the specular reflection associated to the reflection from the element's surface, where the angle of incidence equals the angle of reflectance, and the diffuse reflection associated to a combination of interactions including absorption, transmission, and scattering properties of the illuminated element (Fig. 3.6) [115, 116]. The theory to describe and analyze diffuse reflectance spectra is the Kubelka-Munk theory, which leads to qualitatively results and can be used in quantitative work in many cases.

This method provides information about oxidation state, coordination number, coordination geometry, nature of chemical bonding, degree of condensation, particle size, band gap, nature, and dynamics of surface and adsorbed species [117]. In this work was used an UV/Vis/NIR, PerkinElmer Lambda 1050 spectrophotometer, which is equipped with Tungsten-Halogen and Deuterium lamps. The lamps operate from 175 to 3300 nm with a photomultiplier detector R6872 with a Praying Mantis module. The samples were crushed until a fine powder pieces of a monolith (0.5 g) was obtained. The wavelength range used was from 400 to 800 nm.

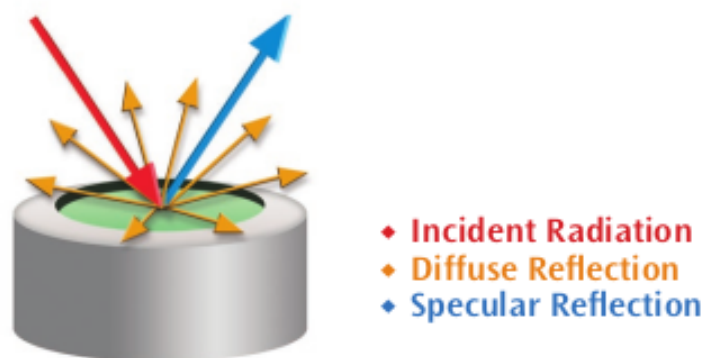


FIGURE 3.6: Illustration of projection of the spectrometer beam into the sample where it is reflected, scattered and transmitted through the sample [116].

### 3.3 Theoretical simulations

The focus of this section is the study of the behavior of the copper (II) in the surface of the silica and chabazite, which is a type of zeolite, through a computational perspective and the contribution of molecular simulations. Typically, the molecular simulation technique used to investigate adsorption in microporous materials is Density Functional Theory. In this work, the simulation code based on Density Functional Theory, plane waves, and pseudopotentials is Quantum Espresso, which is an integrated suite of Open-Source computer codes for electronic-structure calculations and materials modeling at the nanoscale [118].

#### 3.3.1 Quantum Espresso

Quantum Espresso consists of multiple subprograms, including PW (Plane-Wave self-consistent calculation "pw.x"), which is chosen for the simulation.

##### Input file

The input-file consists of multiple main texts, which each one starts with "and sign" (&) and ending with a "slash" (/). The main card of &control, it defines the type of "calculation" where one can calculate the energy of the bonds, optimization of the porous materials using self-consistent calculation "scf" and "relax". The "prefix" is the name prepended to input/output file name, and in the calculations for silica and chabazite were "si" and "chabazite". All auxiliary files will have filename beginning by a prefix. The "outdir" is the directory where input, temporary, output files are

found in this directory. The "pseudo\_dir" is the directory where the value of the pseudo-potentials is found.

The main card of &system defines the information of the system. This defines "ibrav" which is required to define bravais lattice only if the space group is set (integers between 0 to 7). If "ibrav = 0", bravais lattice is defined by the user in CELL\_PARAMETERS card. The "ecutwfc" defines the kinetic energy cutoff (Ry) for wavefunctions. Also, "ecutrho" usually is four times of "ecutwfc" and defines the kinetic energy cutoff (Ry) for charge density and potential. The "nat", defines the number of atoms in the unit cell. The "ntyp", defines the atomic species (see later ATOMIC\_SPECIES). The "nbnd", number of electronic states (bands) to be calculated, in the case of an insulator, "nbnd" is equal to the number of valence bands. The &electrons card defines the information about the convergence as the maximum number of iterations in a "scf" step. ATOMIC\_SPECIES card defines different atoms that users want to use, such as silicon, oxygen, and copper. Also, the atomic weight and the pseudopotentials files are described. ATOMIC\_POSITIONS defines the atomic positions of the atoms in the unit cell. K\_POINTS (automatic) this defines the k.points in the reciprocal lattice. CELL\_PARAMETERS, lattice vectors are found in the cell-matrix in Avogadro software. It depends on the unit lattice vectors such as alat, bohr, and angstrom which is defined in the Avogadro.

### Run a File

The basic commands to run the input defined by serial computation and parallel computation are:

- (i) ./directory/pw.x < file.in > file.out
- (ii) mpirun ./directory/pw.x -procs4 < file.in > file.out

In Figure 3.7 an example of the structure of the input file is shown. The inputs were made in a text editor in Ubuntu software, Quantum espresso version used for simulation is 6.5 and run in parallel computation. All inputs of the detailed information are found in appendix B.

### 3.3.2 Computational methods

The calculations were carried out employing the PWscf code included in the Quantum Espresso package and are based on Density Functional Theory (DFT) [118]. A Standard Solid-State Pseudopotentials (SSSP) library optimized for precision and efficiency were used [119, 120]. Projector Augmented-Wave (PAW) pseudopotentials with Perdew-Burke-Ernzerhof exchange-correlation functional type were used. The

```

&control
  calculation = 'nscf'
  restart_mode='from_scratch',
  prefix='copper'
  outdir='/home/alex/Desktop/qe-6.5-ReleasePack/qe-6.5/
tempdir/'
  pseudo_dir = '/home/alex/Desktop/qe-6.5-ReleasePack/
qe-6.5/PseudoPot/'
/
&system
  ecutwfc = 40,
  ecutrho = 320,
 ibrav= 0,
  nat= 8,
  ntyp= 2,
  nbnd=41
/
&electrons
  conv_thr = 1.0d-8
/
ATOMIC_SPECIES
Cu 63.546 Cu.pbe-dn-kjpaw_psl.1.0.0.UPF
O 15.999 O.pbe-n-kjpaw_psl.1.0.0.UPF

```

ATOMIC_POSITIONS (angstrom)			
Cu	1.16325	0.85250	0.00000
O	-0.21033	1.41856	1.25956
Cu	3.06910	0.85250	2.51912
Cu	3.48975	2.55750	0.00000
Cu	0.74260	2.55750	2.51912
O	-0.63098	1.99144	3.77868
O	2.11617	3.12356	1.25956
O	1.69552	0.28644	3.77868

```

K_POINTS (automatic)
6 6 6 0 0 0
CELL_PARAMETERS {angstrom}
4.65300 0.00000 0.00000
-0.00000 3.41000 0.00000
-0.84130 -0.00000 5.03824

```

FIGURE 3.7: Input file for a  $\text{CuO}$  molecule with the structure for a non self calculation performed in Text editor.

planewave cutoffs kinetic energy were 10 Ry and 40 Ry for the wavefunctions and augmented charge density, respectively. The values were set voluntarily low as it allows to make the calculations on a personal computer. The same calculations with better parameters were also planned to be done on the super computer Quinde. The integration over the Brillouin zone was carried out using gamma k-points. The optimized structures were visualized in the xCrysDen®, which runs on GNU/Linux. This is a crystalline and molecular structure visualization program aiming to display of isosurfaces and contours [121].

## 3.4 Antibacterial analysis

The method used was 10029 membrane filtration [122] for the determination of the quality of the tap water coming from natural sources in Santa Cruz - Galapagos. This water is used for household activities by that Island inhabitants. Moreover, this test was useful to verify the antibacterial activity of the functionalized monoliths with copper.

### 3.4.1 Materials and Reagents

The materials used for the method 10029 membrane filtration were: magnetic stirrer plate, 100 mL, beakers, magnetic bar stirrer, membrane filter, 0.45  $\mu\text{m}$ , Petri dishes with an absorbent pad ( $\phi = 47 \text{ mm}$ ), filtration apparatus with aspirator or pump, forceps, autoclave Biobase Biodustry, BKQ-B50/75100/120 II Model, incubator Pol-Eko-Aparatura, CLN32 STD INOX Model, colonies digital counter Rocker, Galaxy 330. To determine the parameters (pH, temperature, and conductivity), a digital multiparameter HQ40D program was used. Besides, it was necessary to



use buffer standards (pH= 4, 7, and 10). The copper functionalized silica monolith "MonOilCu", and broth ampule of m-ColiBlue24.

### 3.4.2 Experimental procedure

A method was established to determine the quantity of total coliforms and *E. coli* in water samples, thus permitting to evaluate the bactericidal effect of the monoliths put in contact with water samples. First, it was analyzed the blank (original sample of the Cascada water source). Other parameters, such as pH, temperature, and conductivity, were analyzed in the digital multiparameter in this step. After 24 hours of incubation, the grown colonies were counted in the digital counter. To determine the antibacterial activity of the functionalized monoliths, a simple process was developed. The silica monolith called "MonOilCu" was crushed with different grain sizes and labeled as "MonOilCu" A, B, C.

For the *test\_a*, "MonOilCu\_A" the grains were crushed until powder, in the *test\_b* "MonOilCu\_B" was crushed until 3-5 mm of grain size was obtained, and for *test\_c*, "MonOilCu\_C" was crushed until 1-2 mm of grain size was obtained. Then, 30mg of each sample was added separately into three different beakers with 100 mL of tap water from the Hydrant of Cascada Water Source (HCWS). The beaker was placed over a stirring plate with constant stirring for "MonOilCu\_A" and "MonOilCu\_C". Whereas, "MonOilCu\_B" was let in contact with the sample with no stirring. The time contact was 72 hours to measure the monolith activity as a bactericide. After that, the method 10029 membrane filtration was performed, and the resultant colonies were counted in the digital counter. A detailed scheme of the procedure to determine antibacterial activity is presented in Figure 3.8.

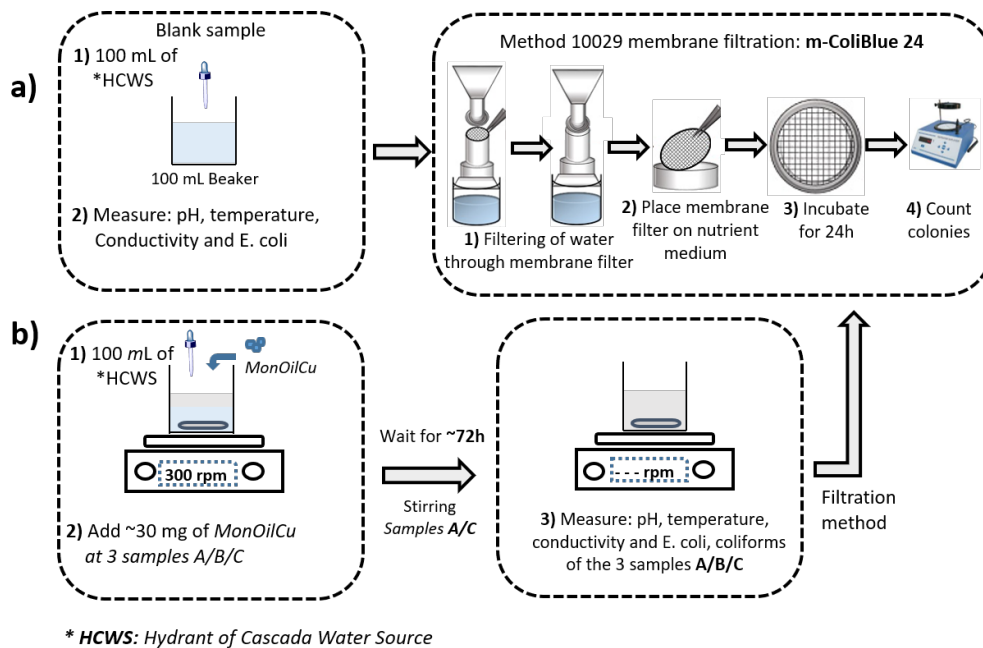


FIGURE 3.8: A scheme of the multiparameter analysis and microbiological test of the HCWS. a) Experimental procedure of the blank sample and b) Experimental procedure of the control water samples with "MonOilCu" (A, B, and C).



## Chapter 4

# Results and Discussion

As previously described, different monoliths were synthesized in order to obtain materials whose main purpose is to decontaminate drinking water by means of bactericidal effects.

### 4.1 Silica monoliths through HIPE method

#### 4.1.1 Scanning Electron Microscope

The silica monolith "Mon1" (Fig. 4.1a) was analyzed by SEM to visualize its hierarchical porosity and morphology in general. In Figure 4.1b, one can differentiate a wide variety of pore sizes in the network of the silica with the naked eye. Through an image processing program called ImageJ, the pore size distribution of "Mon1" was determined.

Mean distribution of pore size of  $1.11 \mu\text{m}$  and a standard deviation of  $1.091 \mu\text{m}$  were determined (Fig 4.1d). The size of this macroporosity would allow big species as *E. coli*, to diffuse without any problem and then to be in contact with mesoporosity where the copper should be present [123]. Instead, mesoporosity helps to maintain a good water diffusion and avoids high-pressure drop in case the monolith would be used as a column it-self. For this purpose, it is also important to have silica walls strong enough to resist the hydraulic pressure generated by the water flux. In Figure 4.1c, one can see that the silica wall is thick (around  $0.5 \mu\text{m}$ ). This wall thickness is kept even after calcination for liberating the mesoporosity, which for sample "Mon1" is occupied by the surfactant template (Pluronic® P123).

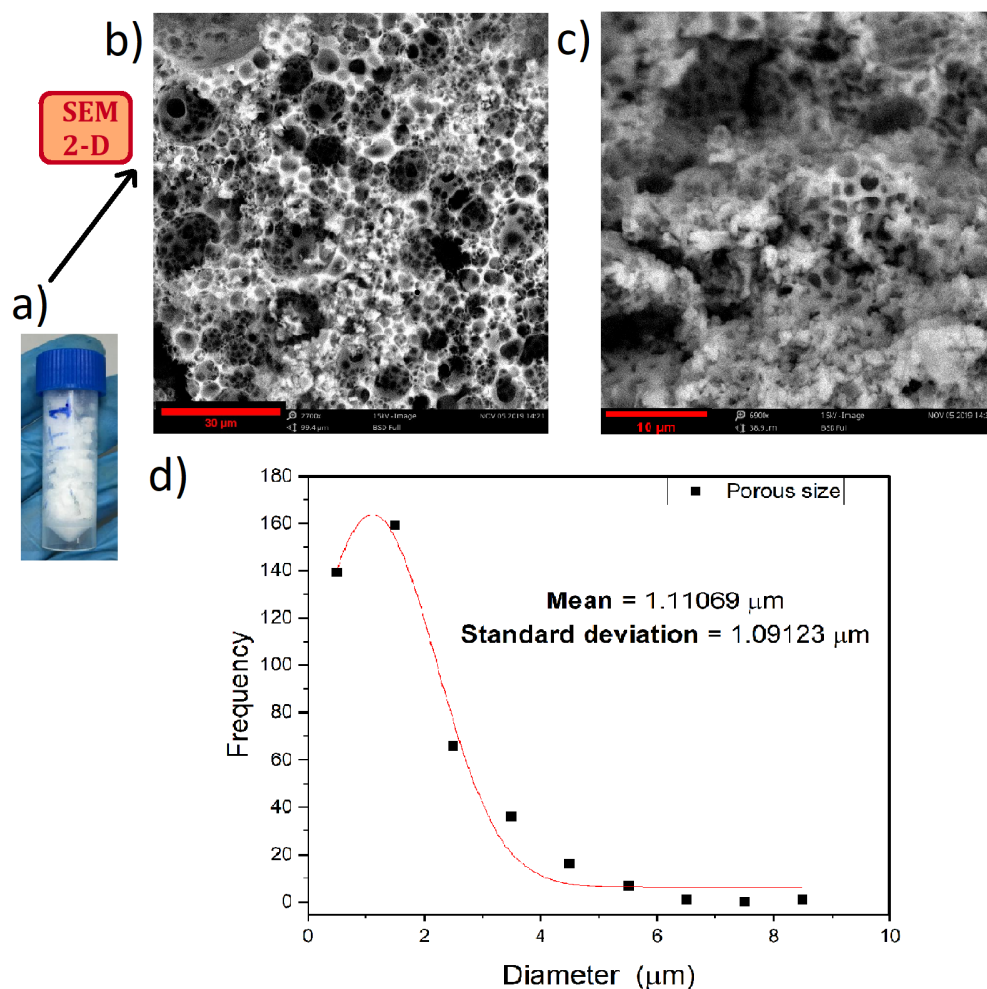


FIGURE 4.1: a) Image of silica monolith by HIPE non calcined "Mon1". b) and c) SEM images of silica monolith "Mon1" at 2700x and 6900x magnification, respectively. d) Distribution of the porosity in the "Mon1" performed in ImageJ.

#### 4.1.2 X-ray Nano-Computed Tomography after calcination

This apparatus was used in order to verify the homogeneity of macroporosity and support the results given by SEM. In this instrument, several images in two dimensions are generated, which, through a meticulous computational analysis and reconstruction work in the instrument software, a 3D image can be constructed such as the one presented in Figure 4.2. Despite carried out for a calcined monolith (Fig. 4.2a), one can see that the macroporosity observed by SEM for a non-calcined monolith is not severely affected. The obtained results help then to confirm that the macropore network of the monolith is formed by a succession of pore windows. This point is particularly important at the moment to use the samples as column microreactors because it will influence the distribution of the hydraulic conductivity affecting the

flow locally. The flow is influenced by the plug homogeneity and isotropy [124]. The Figure 4.2b shows a good porous size distribution where the pores are represented as the dark gray points. Therefore, it seems more pores were liberated after calcination at 500 °C, and the sample was labeled as "Mon2".

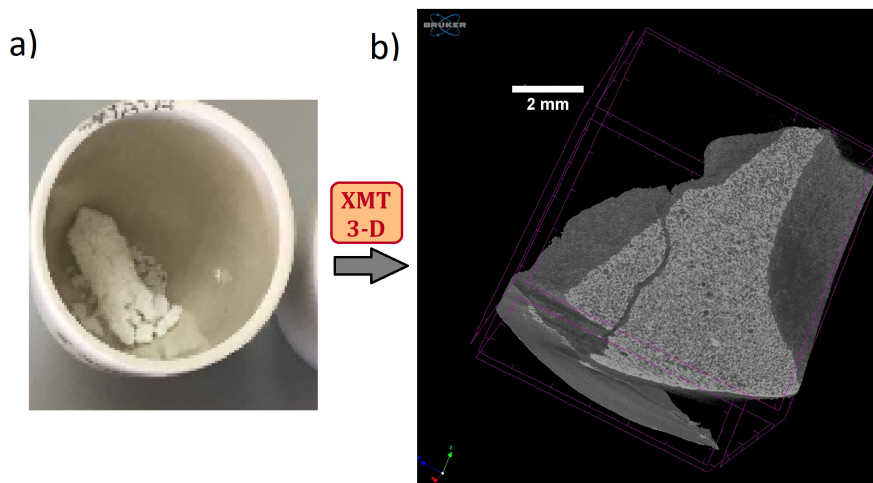


FIGURE 4.2: Images of a) calcined silica monolith synthesized by HIPE "Mon2" and b) nano-computed tomography of "Mon2" where macroporous is visible.

## 4.2 Use of recycled oil as oleic phase for monolith synthesis

As described in the Methodology, a new monolith was synthesized following the same synthetic procedure as for "Mon1" replacing only the oleic phase with recycled cooking oil. After confirming the successful obtention of a monolith, Attenuated Total Reflection FTIR Spectroscopy was used in order to estimate the possible changes occurring when using recycling oil in "MonOil".

The monoliths "Mon1", "MonOil", and "MonOilCu" were analyzed with ATR-FTIR, which is a quick and straightforward method to obtain infrared spectra for monoliths. IR spectra of non-calcined (Mon1), and calcined (MonOil) silica monolith are presented in Figure 4.3.

"Mon1" presents a weak bands at  $3400\text{ cm}^{-1}$  and  $1630\text{ cm}^{-1}$  associated with stretching and bending vibrations of  $H_2O$  molecules respectively (Fig. 4.3a). Therefore, the presence of the Si-OH group is proved as H bonded water. The IR band at  $2865\text{ cm}^{-1}$  corresponds to the flexion vibration of the C-H bond of the surfactant

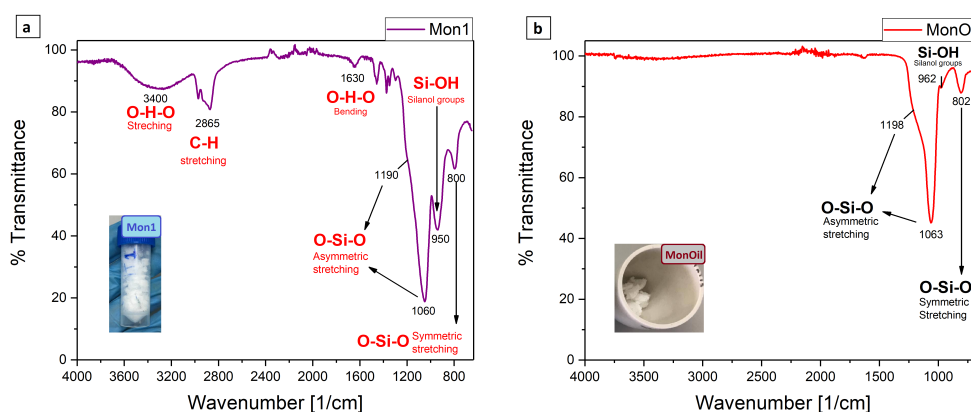


FIGURE 4.3: a) Infrared spectrum of silica monolith "Mon1" in the spectral range associated with bonds of amorphous silica with the respective bands and b) Infrared spectrum of silica monolith "MonOil" in the spectral range associated with bonds of amorphous silica.

Pluronic P123. The very strong peak at  $1060\text{ cm}^{-1}$  with a shoulder at  $1190\text{ cm}^{-1}$  can be assigned for Si-O-Si asymmetric stretching vibrations. The IR band at  $950\text{ cm}^{-1}$  can be assigned for Si-OH groups. The last IR band at  $800\text{ cm}^{-1}$  can be assigned to Si-O-Si symmetric stretching vibrations [125]. In general, the bands before mentioned are similar to the bands of "MonOil" in special silica bonds as O-Si-O asymmetric stretching at  $1198\text{ cm}^{-1}$  and  $1063\text{ cm}^{-1}$  and symmetric stretching vibration at  $802\text{ cm}^{-1}$  (Fig. 4.3b). The IR vibrations of the C-H and O-H bands disappear due to the calcination of this sample at  $500\text{ }^{\circ}\text{C}$ , resulting both in a very low presence of silanol groups [126, 127] and the disappearance of P123.

Once it was proven that the change in oil phase did not interfere in the maintenance of hierarchical structure and homogeneity of macroporous network, the next step was to functionalize the monolith with copper. In order to be able to characterize the monoliths and see the presence of the copper XRD, ATR-FTIR and DRS-UV-Vis were carried out.

## 4.3 Copper functionalization of monolith

### 4.3.1 Physical features of the functionalized silica monolith after calcination

In the functionalization method, the added copper amount was made to keep the  $\text{Cu}/\text{Si}$  molar ratio equal to 0.01. This parameter is very important to maintain precisely for assuring the metal to either be part of the silica network or remain in the

mesoporosity [128]. The addition of the copper results in a blue monolith which then turns green upon drying (Fig. 4.4a) and calcination (Fig. 4.4b). The green color is due to copper oxidation phenomena, and a thin layer called patina is formed. This can be attributed to a change of environment around copper, namely the disappearance of *OH* groups inside the silica network analogous to the presence of water. Consequently, copper is only surrounded by *O* and *Si* atoms generating copper oxide green typical color, and turning into grey color when sample is calcined.

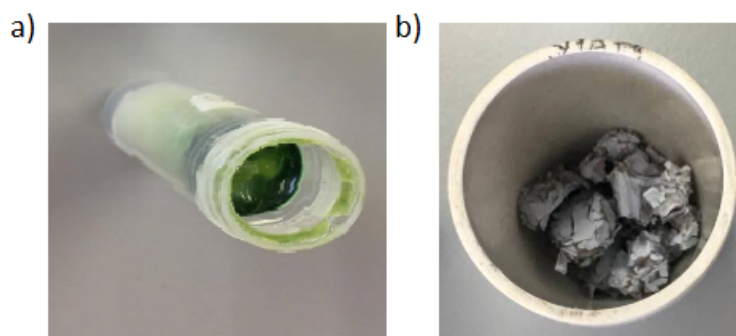


FIGURE 4.4: Images of the functionalized monoliths with copper, a) it was aged by seven days and b) aged seven days and calcined in the muffle furnace with the ramp of 500 °C.

### 4.3.2 X-Ray Powder Diffraction

The X-ray diffraction pattern is important to determine the crystalline structure of materials. However, silica monoliths are known for its amorphous structure, as well as for the majority of silica compounds, because of the lack order in a long scale of its atoms. An amorphous peak with the equivalent Bragg angle at  $2\theta = 23^\circ$  was obtained for amorphous silica in [125] synthesized through the precipitate method while a value of  $2\theta = 21.8^\circ$  through sol-gel method was obtained elsewhere [129]. These values are close to the ones obtained for this work for the samples "MonOil" and "MonOilCu" shown in Figure 4.5.

This research project deals with the obtention of hierarchical silica monoliths by using industrial wastes, therefore, two samples were synthesized the first one with recycled oil to form the macroporosity as previously explained. The second goal was to functionalize the samples with copper (which can also come from industrial activities as waste) to be used in drinking water treatment by eliminating pathogenic bacteria like *E. coli* [130].

The goal of the XRD technique is to determine the copper presence in the silica network of the monolith once calcined ("MonOilCu"). Indeed, the XRD pattern



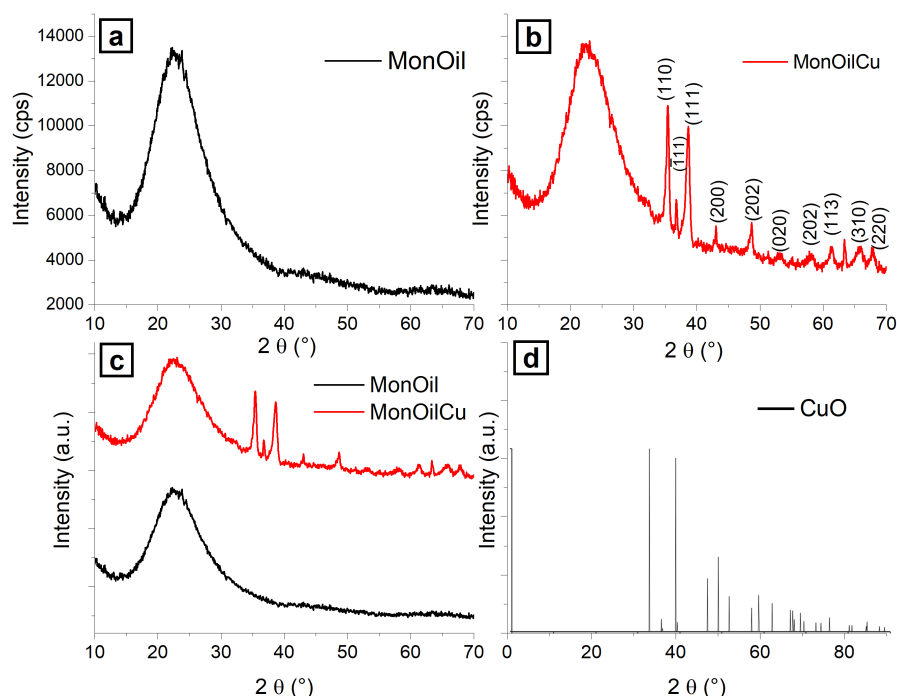


FIGURE 4.5: XRD diffractograms of the silica monoliths. a) XRD spectra of "MonOil" with an amorphous peak, b) XRD spectra of "MonOilCu" which shows a  $CuO$  peaks, c) Offsets of XRD spectrum of "MonOil" and "MonOilCu" and d) Theoretical XRD spectrum of  $CuO$  obtained from GDIS software.

of "MonOilCu" shown in Figure 4.5b is different from the monolith without copper. Therefore, an offset graph of both monoliths is displayed in Figure 4.5c and a clear difference between "MonOil" and "MonOilCu" is visualized. For the non-functionalized monolith is highlighted the well-known pattern for amorphous silica materials where a wide "peak" instead of a sharp peak, typical of high crystalline materials, is present. This wide "peak" has its maximum at an angle of  $2\theta = 22.5^\circ$ . In contrast, the functionalized once calcined presents the sharpened peaks belonging to  $CuO$  besides the wide "peak".

According to the standard  $CuO$  pattern [JCPDS-05-0661], the diffraction patterns are identical to that of pure  $CuO$ , indicating single-phase  $CuO$  formation with monoclinic structure. The  $2\theta$  equal to  $35.40^\circ$ ,  $36.76^\circ$ ,  $38.65^\circ$ ,  $43.05^\circ$ ,  $48.69^\circ$ ,  $53.15^\circ$ ,  $58.12^\circ$ ,  $61.18^\circ$ ,  $66.35^\circ$  and  $68.12^\circ$  appear in the diffractogram for "MonOilCu" which are assignable to (001),  $(\bar{1}11)$ , (111), (200), (202), (020), (202), (113), (310), and (220) crystal planes, respectively. These values were assigned to the reflection lines of monoclinic  $CuO$  nanoparticles in agreement with the diffractogram patterns reported in [131, 132]. Using the Scherrer's formula (eq. A.1) with a K value for monoclinic

structures equal to 1 [133], the average particle size of  $\text{CuO}$  nanoparticles was approximated to  $16.66 \pm 3.33 \text{ nm}$  (Tab.A.1).

The  $\text{CuO}$  diffractogram was compared with a theoretical spectrum obtained by a GDIS software. In Figure 4.5d can be visualized the main peaks which match with the ones of "MonOilCu". When samples are prepared in "one-pot" or a direct synthesis, silicon and metal species can simultaneously condensate around the micelles formed the selected surfactant. Therefore, some of the metal species are most likely trapped in the silica walls during the formation of the final monoliths [134]. According to Delahaye et al. [135] when samples are thermally treated (or calcined), they result in monoliths containing isolated, accessible  $M^{2+}$  species or condensed metal oxides, hydroxides, and salts, depending on the interactions between the organic micelles of P123 and metals. This may influence the unit cell parameters, the wall thickness, and the long-range ordering of the material. Chao et al. [136] concluded that during the hydrothermal synthesis of mesoporous ordered silica (MCM-41) containing vanadium, these ions are grafted on the surface of the walls by condensation with silanol groups. Todorova et al. [137] found out that depending on the quantity of metal loaded, speaking of cobalt for this case, it can be present as M(II) species with tetrahedral coordination or in combination with M(III) species in octahedral symmetry. In most of the cases, all the authors agree with the fact that at higher metal content, part of the metal ions can be eliminated from the framework [135–138].

All those results were achieved thanks to the XRD technique but at small angles ( $2\theta$ , from  $2^\circ$  to  $5^\circ$ ), the main peak at (100) suffers an intensity decrease when other species besides silicon are part of the silica framework. By contrast, metal species introduced by a post-synthetic treatment (template ion exchange, impregnation, grafting, chemical vapor deposition methods) are mostly located at the surface of the mesopores, and they do not modify the internal composition of the silica walls.

Then, for this present work, it was not possible to determine exactly whether copper was part of the silica network or not only using XRD because performed at large angles. However, another way to verify if the metal is part of the framework is the use of FTIR and DRS UV-Vis [135, 138].

### 4.3.3 Diffuse Reflectance of UV-Vis Spectroscopy (DRS-UV-Vis)

Different measurements using the DRS-UV-Vis were developed to analyze the presence of the copper in the silica network. The peaks in the spectrum show the presence of elements in the material structure. The analyzed samples "MonCu" and

"MonOilCu" powder are represented in Figure 4.6. The spectra of both monoliths show a band at about 460 nm to 500 nm, which can be assigned to the copper atom, which matches with the obtained results reported elsewhere [139]. This band is due to the atomic copper cluster. Moreover, the diminished intensity could be assigned to the calcination treatment of the sample "MonOilCu" [139].

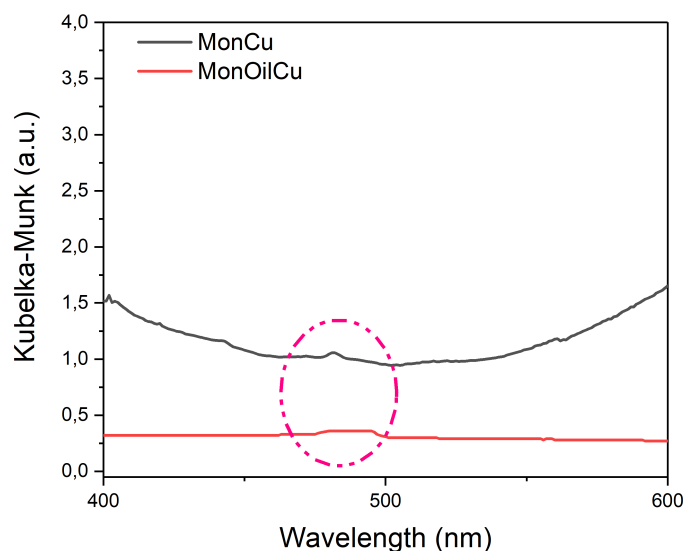


FIGURE 4.6: The UV-Vis diffuse reflectance spectra of "MonCu" and "MonOilCu" silica monoliths.

#### 4.3.4 Attenuated Total Reflection FTIR spectroscopy

The IR spectra of functionalized monolith "MonOilCu" is shown in Figure 4.7. The IR bands for both monoliths "MonOil" and "MonOilCu" are quite similar because there is no presence of the C-H bond due to the calcination process. However, it has very weak IR bands at  $3400\text{ cm}^{-1}$  and  $1630\text{ cm}^{-1}$  assigned to stretching and bending vibrations of  $H_2O$ . Thus, "MonOilCu" monolith has more silanol groups than "MonOil," and the bands of O-Si-O symmetric and asymmetric were shifted around  $7\text{ cm}^{-1}$  to the left. A reason for this could be the presence of the copper in the silica network [138, 140]. According to literature, the IR bands of the copper appear at around  $454.5\text{ cm}^{-1}$  and  $605.7\text{ cm}^{-1}$  and can be assigned to the Cu-O stretching vibration [131, 132]. The bands at  $525\text{ cm}^{-1}$  and  $580\text{ cm}^{-1}$  indicated the formation of the  $CuO$  nanostructure. However, "MonOilCu" IR spectra were recorded in a range between  $4000\text{ cm}^{-1}$  to  $650\text{ cm}^{-1}$ , where these bands could not be observed in this work.

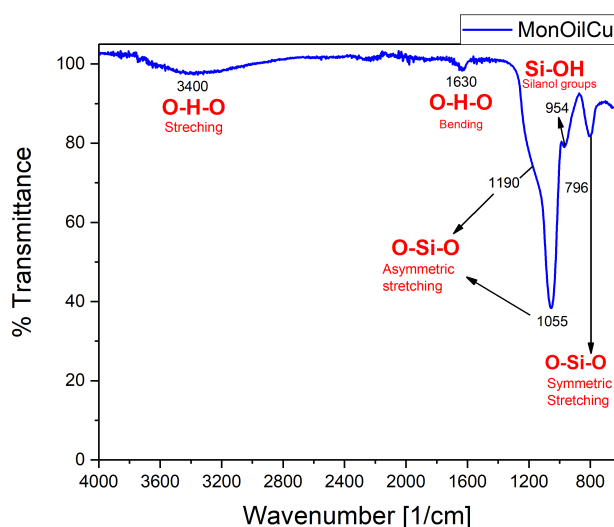


FIGURE 4.7: Infrared spectrum of silica monolith "MonOilCu" in the spectral range associated with bonds of amorphous silica.

### 4.3.5 Conclusions on the experimental synthesis and characterization

It can be said that the samples present the typical hierarchical morphology of its pores observed in silica monoliths obtained by HIPE [97]. The change in the oil-phase did not affect these features in the samples, as it can be seen by SEM and Nano-Computed Tomography (Figures 4.1, 4.2). The functionalized monoliths with copper turned out in a combination of copper oxide particles and nanoparticles along with the silica after calcination according to the results given by XRD and DRS-UV-Vis and compared with literature [139] (Figures 4.5, 4.6, 4.15). By ATR-FTIR, one can observe the main functional groups belonging to silica and  $CuO$  for the different monoliths (Figures 4.3, 4.7).

## 4.4 Theoretical simulations

The study of the copper behavior on the silica surface and chabazite was done through calculations using Quantum Espresso. The main goal was to know the formation of the possible bond on the silicon surface and chabazite. The first input, which is the basis-set of the material to simulate, was the silicon surface with a copper close to the surface in just one position (fig. 4.8a). In the context of this work, a

flat surface (a slab in the calculations) would be a representative model of a macropore as the curvature would be almost flat. Moreover the type of atoms would mimic the chemical nature of the macroporous surface.

On the other hand, the pure silica chabazite (*chab*) was chosen because it is a porous material that contains exclusive silicon and oxygen atoms. Therefore, it can emulate the behavior of silica monolith because it has the same type of atoms. Thus, the copper atom was placed in three different sites over the *chab* structure as shown in the left, middle, and right side (Figures 4.9a, 4.10a, 4.11a). The objective is to study a simple unit cell for pure silica chabazite to future works, build a slab to obtain a large structure, and determine the behavior of copper in a network of porous silica.

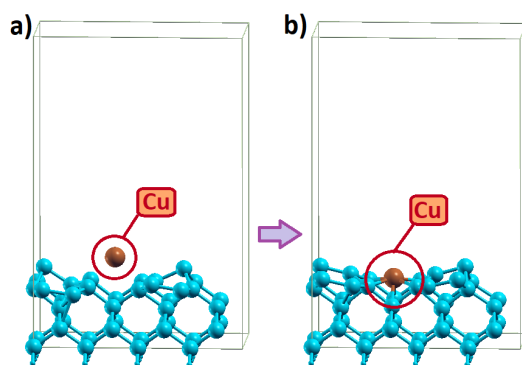


FIGURE 4.8: A ball-and-stick model for copper adsorbed on pure silica surface [100] interface (*Si*: light blue, and *Cu*: orange).

The case for copper atom adsorbed on the pure silica surface takes its position on the hollow site in between the two silicon atoms (4.8b). The copper atom forms covalent bonds with silicon of 2.525, 2.615, 2.624, 2.669, 2.623, 2.629 Å. The binding energy ( $E_b$ ) is also calculated as the difference in total energy by the next equation:

$$E_b = E(Si - Cu_{configuration}) - E(Si_{bulk}) - E(Cu_{atom})/area \quad (4.1)$$

Where  $E(Si - Cu_{configuration})$  is the total energy of the optimized copper atom adsorbed on the surface of *Si*,  $E(Si_{bulk})$  represents the total energy of the bulk *Si* system, and  $E(Cu_{atom})$  is the total energy of the isolated copper atom [89]. The calculated value of binding energy for copper adsorbed on silica surface (fig. 4.8a) is -1384.71 kJ/mol. After optimization, copper interacts with the down atom of the buckled surface silicon dimers in this configuration.

The calculation of binding energy for pure silica chabazite simulation used the same formula explained above, and the results obtained for the three positions of copper in *chab* surface (Figures 4.9b, 4.10b, 4.11b), were -3089.45, -2713.06, -2897.55

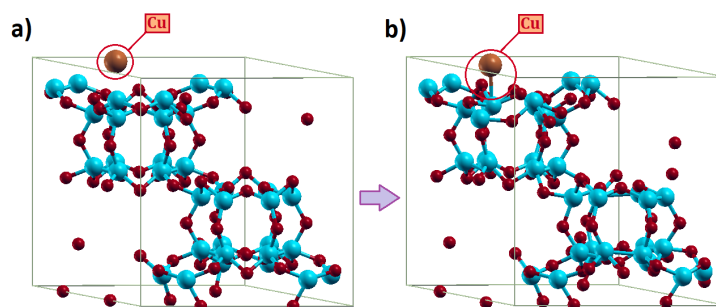


FIGURE 4.9: A ball-and-stick model for copper absorbed at left position of pure silica chabazite unit cell surface [100] interface (O: red, Si: light blue, and Cu: orange).

$\text{kJ/mol}$ . The minimum and maximum Cu-O distance observed is 1.56 and 2.7 Å, respectively. Moreover, the results obtained for the bonds formed between copper and *chab* unit cell are represented in table 4.1. These result suggest that copper at the position in fig. 4.9b is more stable than others, it could be due to a preferential site in the monolith.

Therefore, the copper simulation in the surface shows good results because the copper atom can be bonded with silicon or oxygen atoms, forming copper oxide (fig. 4.10b).

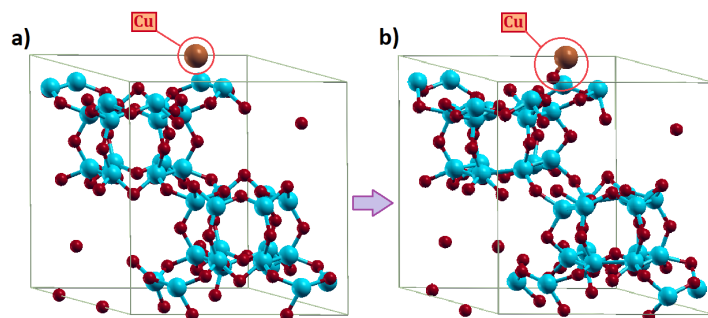


FIGURE 4.10: A ball-and-stick model for copper absorbed at center position of pure silica chabazite unit cell surface [100] interface (O: red, Si: light blue, and Cu: orange).

Moreover, the bonds between copper and oxygen are in agreement with the values reported in [141]. Although binding energy for the *chab* and silica surface did not match with the reported, it could be resolved to increase the kinetic cut-off energies to run in clusters with more processors [142, 143]. Therefore, the simulations' results confirm a possible bonding between copper, oxygen, and silica. The change

induced by the presence of copper on the structure seems to confirm the shift previously observed in the IR spectra. Moreover, a higher energy observed in the case of the chabazite suggests that copper is probably more present inside smaller porosities, corresponding in our material to mesopores.

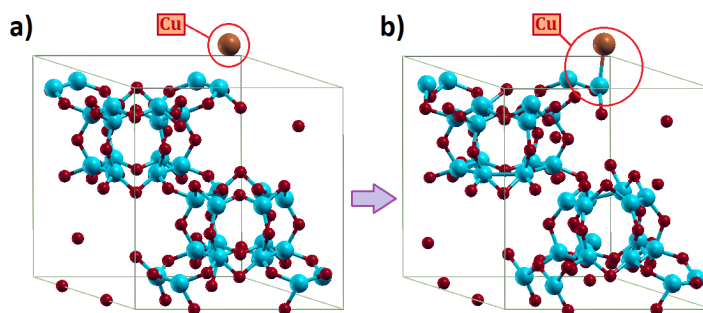


FIGURE 4.11: A ball-and-stick model for copper adsorbed at right position of pure silica chabazite unit cell surface [100] interface (O: red, Si: light blue, and Cu: orange).

TABLE 4.1: Listing of bond-length for copper adsorbed and close atoms of pure silica chabazite interface.

Order	Bond-length ( Å )	Order	Bond-length ( Å )
Cu(109)-Si(98)	2.701	Cu(109)-Si(77)	3.2088
Si(80)-Si(98)	3.5979	Cu(109)-Si(107)	5.481
Cu(109)-O(52)	2.7096	Cu(109)-Si(81)	4.67
O(18)-Si(98)	2.081	Cu(109)-Si(77)	2.774
Si(98)-O(27)	2.1009	O(43)-Si(77)	2.0839
Si(98)-Si(106)	2.3133	O(26)-Si(77)	2.3067
Cu(109)-O(53)	1.5691	O(9)-Si(77)	2.059

## 4.5 Antibacterial test

The copper (II) oxide has been known in the last decades for their microbiological activity in the experiments carried out with this compound. Previously it was shown the presence of copper in the silica framework of the sample "MonOilCu" by DRUV-UV-Vis and ATR-FTIR. This encourages this research work to perform the bactericidal experiments for eliminating *E. coli* from tap water coming from "La cascada" hydrant.

The method 10029 membrane filtration (HATCH), as it was already explained, is the most used in the quality water labs in Ecuador, and it was chosen in this work. The hydrant of water source was analyzed in the Santa Cruz-Galapagos because the water quality of this hydrant is not allowed for household activities and human consumption. Therefore, the method 10029 membrane filtration (HATCH) was performed in the aim to determine the total coliforms and *E. coli* presence in the water sample without "MonOilCu" treatment. Furthermore, parameters such as pH, temperature, and conductivity were measured, and they are reported in Table 4.2.

TABLE 4.2: Initial parameters measurements of three samples of water (HWCS) and results of the microbiological test.

Sample	Stirring	pH	Temp (°C)	Conductivity ( $\mu\text{S}/\text{cm}$ )	<i>E. coli</i>	Total coliforms
Sample_a	Yes	7.63	24.9	1653	presence	1387
Sample_b	No	7.6	25	1654	presence	1387
Sample_c	Yes	7.63	25.1	1655	presence	1387

In Figure 4.12, the presence of the *E. coli* and limited exceed of total coliforms for drinking water were found in the results for the water sample without treatment. Moreover, the results of the treatment of the drinking water with the "MonOilCu" are reported in Table 4.3.

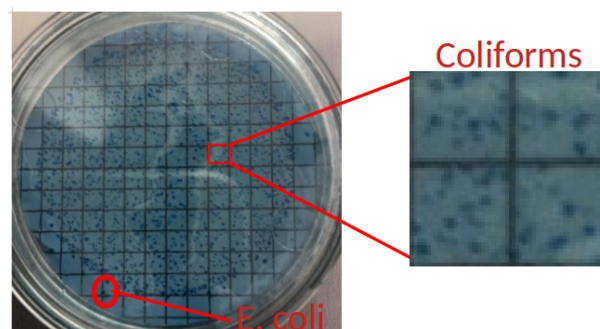


FIGURE 4.12: Image of the membrane filtration result from the hydrant cascada water source without "MonOilCu" treatment where *E. coli* and coliforms are present in high quantity.

The obtained results for the antibacterial activity depend on the grain size of the silica monolith used and the constant stirring. The **test-b** with a big size grain and without stirring highlights the lowest number of microbiological colonies in comparison with the monolith of **test-a** and **test-c**. In Figure 4.13, one can appreciate



these results in a better way. The antimicrobial action of  $CuO$  particles embedded in silica porous is shown in Figure 4.14. The elimination of bacteria *E. coli* involves an environment of copper ions. It means that the copper ion is coordinated by four and six oxygen atoms, creating a tetrahedral and octahedral environment. Besides, the copper ions migration into the water is limited to this coordination. Thus, the increase of conductivity while the "MonOilCu" is in the sample water is agreed with the copper ions environment [144].

TABLE 4.3: Parameters measurements after 72 hours treated with "MonOilCu" of three samples of water (HCWS) and results of the microbiological test.

Sample	pH	Temp (°C)	Conductivity ( $\mu S/cm$ )	<i>E. coli</i>	Total coliforms
Sample_a	8.53	31	2175	presence	1
Sample_b	8.17	25	1835	absence	65
Sample_c	8.25	31	2181	presence	10

Therefore, this experiment confirms the antibacterial activity of the monolith "MonOilCu". Furthermore, this suggests the possible application of monolith as depolluting water material for water decontamination purposes, and the significant advantage is the short time synthesis and the non-expensive procedure and materials to make it.

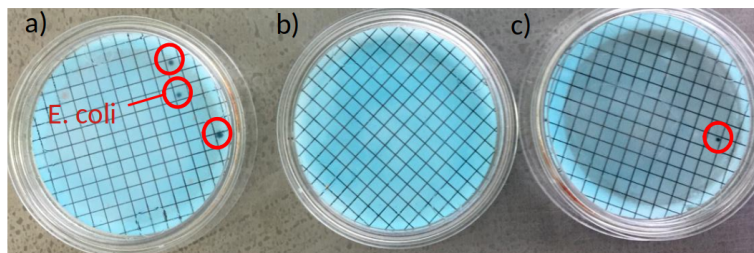


FIGURE 4.13: Images of the membrane filtration results from the hydrant cascade water source with "MonOilCu" treatment where *E. coli* and coliforms diminished.

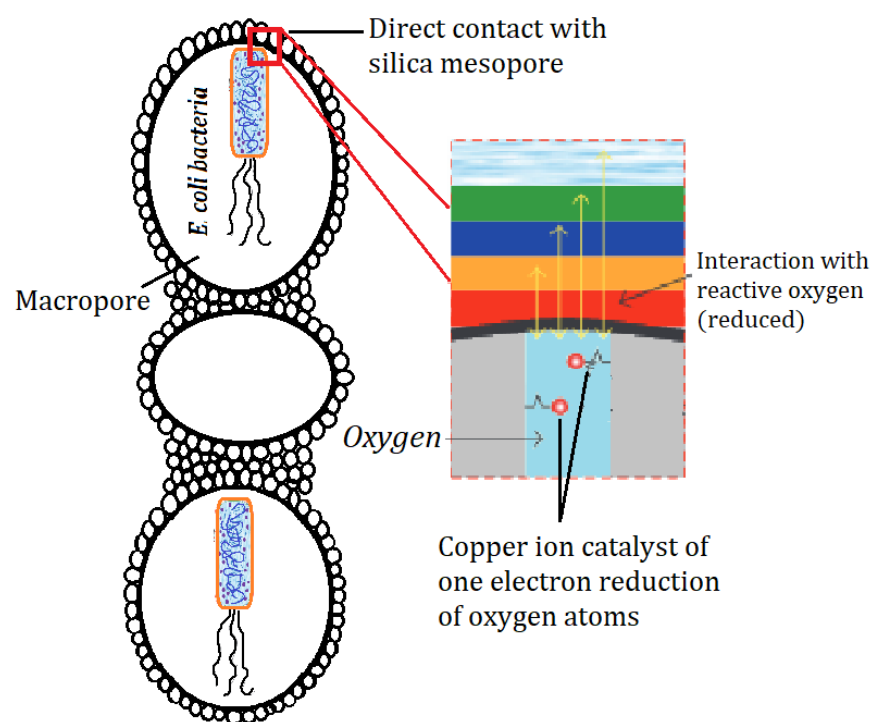


FIGURE 4.14: Schematic representation of antimicrobial action of "MonOilCu" against *E. coli* bacteria adapted from [144].

### 4.5.1 Material resistance after the test evaluated by DRS-UV-Vis

The silica monolith "MonOilCu" was used to microbiological tests, and it was kept after the experiment. DRS-UV-Vis measurements were carried out for that sample to verify if the copper oxide was kept in the network, and it was compared with the sample before the experiment (Figure 4.15). The data were normalized (0-1) in order to appreciate the copper presence. From around 450 nm to 500 nm and a weak peak from 500 nm to 600 nm are attributed for the atomic copper cluster and plasmon resonance band that suggest the presence of *CuO* nanoparticles. As a result, the peaks appeared in the same range for all samples and indicated the *CuO* presence in the silica network. Therefore, the intensity of the spectra shows the concentration of the *CuO* nanoparticles qualitatively because these after thermal treatment have a highly dispersed spatial distribution in the silica framework. Then, *CuO* nanoparticles are not in the same concentration around the silica monolith.

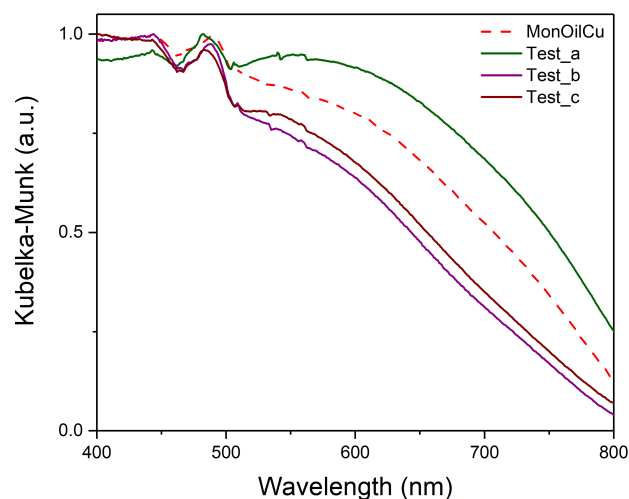


FIGURE 4.15: The UV-Vis diffuse reflectance spectra of "MonOilCu" silica monoliths used in three different tests (a, b, c) in microbiological test.

## Chapter 5

# Conclusions and future work

Depending on the different industries and household practices, different contaminations could be encountered in water, and this is a major problem in rural areas where water treatment installations are usually not present. The main objective of this work was to demonstrate the possibility of constructing interesting materials using the pollution present in water, as examples recycled cooking oil and copper. In this work, the first part was focused on the synthesis of a silica monolith via the well-established HIPE method.

The morphology and hierarchical nature of the obtained monolith were proven and served us to establish a reference for the subsequent modified monolith. Indeed, Scanning Electron Microscopy confirms the hierarchical porosity of monolith while a well-distributed porosity of the calcined silica monolith was observed in the Nano-Computed Tomography images. X-ray Powder Diffractometer allows to confirm the typical broad peak at around  $2\theta = 24^\circ$ , typical of amorphous silica materials. Once the method was confirmed, a modification of the synthetic procedure was done through the replacement of the oleic phase by recycled cooking oil. Interestingly, a monolith was also obtained in that case.

Apart from the porous structure obtained, the ATR-FTIR was a special technique to evaluate the similarity in bonding pattern between the normal monolith, and the one obtained using recycled cooking oil. In that sense, O-Si-O asymmetric and symmetric stretching vibrations, observed at  $1052\text{ cm}^{-1}$  and  $1190\text{ cm}^{-1}$ , respectively, were particularly important to establish a similar bonding nature between both monoliths. Moreover, ATR-FTIR spectra can characterize the calcination process where the disappearance of C-H vibration corresponds to the removal of the surfactant, and O-H band disappearance corresponds to the removal of silanol groups. The second aspect investigated was the functionalization of this monolith with copper. While a small quantity is introduced during the synthesis, a monolith with a characteristic color of copper was obtained. The presence of copper in the material was confirmed in XRD through the appearance of sharp peaks at around

$2\theta = 35^\circ, 37^\circ$ . Diffuse Reflectance Spectroscopy UV-Vis also gave important information of the peak at around 475 - 500 nm, which can suggest copper in a specific environment. Moreover, using ATR-FTIR, a small shift of the silanol band to the left of  $7 \text{ cm}^{-1}$  is found, suggesting that copper directly affects the O-Si-O bonding.

The theoretical calculations, realized with Quantum Espresso, confirm this trend as copper shows a high affinity for Si or O atoms, concomitant with slight deformation of the chabazite model when copper is present. In fact, copper can establish a bond with the surface. Theoretical calculations also suggest that copper is present in more confined porosities rather than in the biggest macroporosity through the analysis of the three sites intended in the chabazite structure. From this information, we can conclude that copper probably forms bonds with the silica framework rather than remaining through a weak adsorption process.

Finally, an antibacterial analysis was performed in order to evaluate the depolluting efficiency of this copper functionalized monolith for water samples in Santa Cruz. Indeed, functionalized monolith (MolOilCu) shows a very good performance for the remotion of *E. coli bacteria* in the samples, which is known as one of the main characteristics of copper oxide reported in the literature. DRS-UV-Vis, before and after carrying out the antibacterial test, was useful to determine if the copper is liberated and if the copper undergoes a redox change upon decontamination. The spectra of the "MonOilCu" after the test display the same peak assigned for the copper reflecting a certain stability of the material. This information is precious as it can suggest that it could be reusable at different times but should be explored more deeply in the future. The work of this thesis shows a promising route: use pollution to fabricate depolluting materials. As a perspective, more research effort could be devoted to this kind of material.

# Appendix A

## Data analysis

### A.1 Crystalline structure of CuO nanoparticles

The average particle size of *CuO* nanoparticles was calculated using the Scherrer's formula which is described below. The observed XRD peak broadening could come from the crystallite size (Scherrer's formula) [133]. For the best accuracy, extract the size broadening  $\beta_{size}$  from the observed  $\beta_{obs}$ .

$$D_p = \frac{K\lambda}{B\cos(\theta)} \quad (\text{A.1})$$

$D_p$  : Average crystalline size (nm)

$K$  : Scherrer constant.  $K$  varies from 0.68 to 0.28.  $K = 0.94$  for spherical crystallites with cubic symmetry.

$\lambda$  : X-ray wavelength. For mini XRD, Cu  $K\alpha$  average = 1.54178 Å

$\beta_{size}$ : FWHM ( Full Width at Half Maximum ) of XRD peak.

$\theta$  : XRD peak position, once half of  $2\theta$

TABLE A.1: XRD peaks data of silica monolith "MonOilCu" for calculation of the average crystalline size of *CuO* nanoparticles.

Peak position $2\theta(^{\circ})$	FWHM $B_{size} (^{\circ})$	$D_p$	$D_p$ Average (nm)
35.40	0.551	16.881	16.66
36.76	0.469	19.944	
38.65	0.463	20.494	
43.05	0.502	20.494	
48.69	0.565	17.468	
53.15	0.596	16.943	
58.12	0.568	18.052	
61.18	0.636	16.543	
65.94	1.061	10.028	
67.89	0.804	10.978	



## Appendix B

# Computational files

## B.1 Input codes for simulations of copper adsorption on silica and pure chabazite surfaces

```

&control
  calculation = 'relax',
  restart_mode = 'from_scratch',
  prefix = 'si_surfb',
  | pseudo_dir = '/home/alex/Desktop/qe-6.5-ReleasePack/qe-6.5/
PseudoPot/'
  outdir = '/home/alex/Desktop/qe-6.5-ReleasePack/qe-6.5/tempdir/'
  etot_conv_thr = 5.0d-5,
  forc_conv_thr = 5.0d-4
/
&system
 ibrav = 8, celldm(1) = 29.2337482, celldm(2) = 0.5, celldm(3) = 1.5,
nat = 57,
ntyp = 3,
ecutwfc = 10,
ecutrho = 40,
occupations = 'smearing', smearing = 'gaussian', degauss = 0.005,
nosym = .true.
/
&electrons
  mixing_beta = 0.7,
  conv_thr = 1.0d-7
/
&ions
  ion_dynamics = "bfgs",
/
ATOMIC_SPECIES
Si 28.0855 Si.pbe-n-kjpaw_psl.1.0.0.UPF
H 1.00784 H_ONCV_PBE-1.0.oncvpsp.upf
Cu 63.546 Cu.pbe-dn-kjpaw_psl.1.0.0.UPF

ATOMIC_POSITIONS (alat)
!From avogadro library

K_POINTS (gamma)

```

FIGURE B.1: Parameters used in the simulation for copper adsorption on silica surface.



---

```

&control
  calculation = 'relax'
  restart_mode='from_scratch',
  prefix='chabcu',
  outdir='/home/alex/Desktop/qe-6.5-ReleasePack/qe-6.5/tempdir/'
  pseudo_dir = '/home/alex/Desktop/qe-6.5-ReleasePack/qe-6.5/
PseudoPot/'
/

&system
  ecutwfc = 10,
  ecutrho = 40,
 ibrav= 0,
  nat= 109,
  ntyp= 3,
  ! nbnd= 288
  occupations= 'smearing', smearing='gaussian', degauss= 0.005
/

&electrons
  diagonalization='david'
  conv_thr=1e-8
/

&ions
  ion_dynamics="bfgs",
/

ATOMIC_SPECIES
Si 28.086 Si.pbe-n-kjpaw_psl.1.0.0.UPF
O 15.999 O.pbe-n-kjpaw_psl.1.0.0.UPF
Cu 63.546 Cu.pbe-dn-kjpaw_psl.1.0.0.UPF
ATOMIC_POSITIONS (angstrom)
!From avogadro library|
K_POINTS {gamma}

CELL_PARAMETERS {angstrom}
13.67500 0.00000 0.00000
-6.83750 11.84290 0.00000
-0.00000 -0.00000 14.76700

```

---

FIGURE B.2: Parameters used in the simulation for copper adsorption at position A on pure silica chabazite surface.

```
&control
  calculation = 'relax'
  restart_mode='restart',
  prefix='chab',
  outdir='/home/alex/Desktop/qe-6.5-ReleasePack/qe-6.5/tempdir/'
  pseudo_dir = '/home/alex/Desktop/qe-6.5-ReleasePack/qe-6.5/
PseudoPot/'
/

&system
  ecutwfc = 10,
  Ecutrho = 40,
  ibrav= 0,
  nat= 109,
  ntyp= 3,
  ! nbnd= 288
  occupations= 'smearing', smearing='gaussian', degauss= 0.005
/

&electrons
  diagonalization='david'
  conv_thr=1e-8
/

&ions
  ion_dynamics="bfgs",
/

ATOMIC_SPECIES
Si 28.086 Si.pbe-n-kjpaw_psl.1.0.0.UPF
O 15.999 O.pbe-n-kjpaw_psl.1.0.0.UPF
Cu 63.546 Cu.pbe-dn-kjpaw_psl.1.0.0.UPF
ATOMIC_POSITIONS (angstrom)
!From avogadro
K_POINTS {gamma}

CELL_PARAMETERS {angstrom}
13.67500 0.00000 0.00000
-6.83750 11.84290 0.00000
-0.00000 -0.00000 14.76700
```

---

FIGURE B.3: Parameters used in the simulation for copper adsorption at position B on pure silica chabazite surface.

```

&control
  calculation = 'relax'
  restart_mode='from_scratch',
  prefix='chab',
  outdir='/home/alex/Desktop/qe-6.5-ReleasePack/qe-6.5/tempdir/'
  pseudo_dir = '/home/alex/Desktop/qe-6.5-ReleasePack/qe-6.5/
PseudoPot/'
/

&system
  ecutwfc = 10,
  Ecutrho = 40,
 ibrav= 0,
  nat= 109,
  ntyp= 3,
  occupations= 'smearing', smearing='gaussian', degauss= 0.005
/

&electrons
  diagonalization='david'
  conv_thr=1e-8
/

&ions
  ion_dynamics="bfgs",
/

ATOMIC_SPECIES
Si 28.086 Si.pbe-n-kjpaw_psl.1.0.0.UPF
O 15.999 O.pbe-n-kjpaw_psl.1.0.0.UPF
Cu 63.546 Cu.pbe-dn-kjpaw_psl.1.0.0.UPF
ATOMIC_POSITIONS (angstrom)
!From avogadro library|
K_POINTS {gamma}

CELL_PARAMETERS {angstrom}
13.67500 0.00000 0.00000
-6.83750 11.84290 0.00000
-0.00000 -0.00000 14.76700

```

FIGURE B.4: Parameters used in the simulation for copper adsorption at position C on pure silica chabazite surface.

# Bibliography

- (1) Culp, J. T. *Elsevier B.V* **2015**, 149–176.
- (2) Zhang, J.; Chen, J.; Peng, S.; Peng, S.; Zhang, Z.; Tong, Y.; Miller, P. W.; Yan, X.-P. *Chem. Soc. Rev.* **2019**, *48*, 2566–2595.
- (3) Cambor, M.; Villaescusa, L.; Cabañas, M. *Topics in Catalysis* **1999**, *9*, DOI: 10.1023/a:1019154304344.
- (4) Tikkanne, A. Chabazite, <https://www.britannica.com/science/chabazite>, 2019.
- (5) M. Moshoeshe M. S. Nadiye-Tabbiruka, V. O. *American Journal of Materials Science* **1998**, *69*, 196–221.
- (6) Kulprathipanja, S., *Zeolites in industrial separation and catalysis*; John Wiley & Sons: 2010, pp 61–68.
- (7) Martín, N.; Moliner, M.; Corma, A. *Chem. Commun.* **2015**, *51*, 9965–9968.
- (8) Cundy, C. S.; Cox, P. A. *Microporous and Mesoporous Materials* **2005**, *82*, 1–78.
- (9) Ng, E.-P.; Zou, X.; Mintova, S., *Environmental Synthesis Concerns of Zeolites*; Suib, S. L., Ed.; Elsevier: 2013.
- (10) Jones, C.; Tsuji, K.; Takewaki, T.; Beck, L.; Davis, M. *Microporous and Mesoporous Materials - MICROPOROUS MESOPOROUS MAT* **2001**, *48*, 57–64.
- (11) Pan, T.; Wu, Z.; Yip, A. C. *Catalysts* **2019**, *9*, 274.
- (12) Goel, S.; Zones, S. I.; Iglesia, E. *Chemistry of Materials* **2015**, *27*, 2056–2066.
- (13) Jin, Y.; Chen, X.; Sun, Q.; Sheng, N.; Liu, Y.; Bian, C.; Chen, F.; Meng, X.; Xiao, F.-S. *Chemistry – A European Journal* **2014**, *20*, 17616–17623.
- (14) Aono, H.; Takeuchi, Y.; Itagaki, Y.; Johan, E. *Solid State Sciences* **2020**, *100*, 106094.
- (15) Díaz-Cabañas, M.-J.; A. Barrett, P. *Chem. Commun.* **1998**, 1881–1882.
- (16) Dang, L.; Le, S.; Lobo, R.; Pham, T. *Journal of Porous Materials* **2020**, DOI: 10.1007/s10934-020-00923-y.
- (17) Govender, S.; Friedrich, H. *Catalysts* **2017**, *7*, 62.

- (18) Tanaka, N.; Unger, K. K., *The Basic Idea and the Drivers*; John Wiley Sons, Ltd: 2011; Chapter 1, pp 1–7.
- (19) Nakanishi, K., *Synthesis Concepts and Preparation of Silica Monoliths*; John Wiley Sons, Ltd: 2011; Chapter 2, pp 9–33.
- (20) Skudas, R.; Thommes, M.; Unger, K. K., *Characterization of the Pore Structure of Monolithic Silicas*; John Wiley Sons, Ltd: 2011; Chapter 4, pp 47–80.
- (21) Barut, M.; Podgornik, A.; Merhar, M.; Štrancar, A., *Chapter 3 - Short Monolithic Columns Rigid Disks*; Švec, F., Tennikova, T. B., Deyl, Z., Eds.; Journal of Chromatography Library, Vol. 67; Elsevier: 2003, pp 51 –75.
- (22) Švec, F.; Tennikova, T. B., *Chapter 1 - Historical Review*; Švec, F., Tennikova, T. B., Deyl, Z., Eds.; Journal of Chromatography Library, Vol. 67; Elsevier: 2003, pp 1 –15.
- (23) Strancar, A.; Podgornik, A.; Barut, M.; Necina, R., *Short Monolithic Columns as Stationary Phases for Biochromatography*; Freitag, R., Ed.; Springer Berlin Heidelberg: Berlin, Heidelberg, 2002, pp 49–85.
- (24) Malik, A. *Electrophoresis* **2002**, *23*, 3973–3992.
- (25) Branovic, K; Lattner, G; Barut, M; Strancar, A; Josic, D.; Buchacher, A *Journal of Immunological Methods* **2002**, *271*, 47 –58.
- (26) Miyazaki, S.; Takahashi, M.; Ohira, M.; Terashima, H.; Morisato, K.; Nakanishi, K.; Ikegami, T.; Miyabe, K.; Tanaka, N. *Journal of Chromatography A* **2011**, *1218*, Selected Papers of 35th International Symposium on High Performance Liquid Phase Separations and Related Techniques, 1988 –1994.
- (27) Cabrera, K. Recent Advances in Silica-Based Monolithic HPLC Columns, <http://www.chromatographyonline.com/recent-advances-silica-based-monolithic-hplc-columns?id=&pageID=1&sk=&date=>, 2008.
- (28) ŠVEC, F.; FRÉCHET, J. M., *Chapter 2 - Rigid Macroporous Organic Polymer Monoliths Prepared by Free Radical Polymerization*; Švec, F., Tennikova, T. B., Deyl, Z., Eds.; Journal of Chromatography Library, Vol. 67; Elsevier: 2003, pp 19 –50.
- (29) Buchmeiser, M. R. *Polymer* **2007**, *48*, 2187 –2198.
- (30) Weed, A.-M. K.; Dvornik, J.; Stefancin, J. J.; Gyapong, A. A.; Svec, F.; Zajickova, Z. *Journal of Separation Science* **2013**, *36*, 270–278.
- (31) Mistry, K.; Grinberg, N. *Journal of Liquid Chromatography & Related Technologies* **2005**, *28*, 1055–1074.
- (32) Cabrera, K. *Journal of separation science* **2004**, *27*, 843–52.

- (33) Lu, J.; Ye, F.; Zhang, A.; Wei, Z.; Peng, Y.; Zhao, S. *Journal of separation science* **2011**, *34*, DOI: 10.1002/jssc.201100102.
- (34) Schwieger, W.; Machoke, A. G.; Weissenberger, T.; Inayat, A.; Selvam, T.; Klumpp, M.; Inayat, A. *Chem. Soc. Rev.* **2016**, *45*, 3353–3376.
- (35) Sun, M.-H.; Huang, S.-Z.; Chen, L.-H.; Li, Y.; Yang, X.-Y.; Yuan, Z.-Y.; Su, B.-L. *Chem. Soc. Rev.* **2016**, *45*, 3479–3563.
- (36) YANG, P., *Chapter 14 - Ordered Inorganic Structures*; Švec, F., Tennikova, T. B., Deyl, Z., Eds.; *Journal of Chromatography Library*, Vol. 67; Elsevier: 2003, pp 301–322.
- (37) AU Sun M., C. C.-C. L. S. B. *Frontiers of Chemical Science and Engineering* **2016**, *10*, 301–347.
- (38) Ming-Hui, S.; Huang, S.; Chen, L.-H.; Li, Y.; Yang, X.-Y.; Yuan, Z.-Y.; Su, B.-L. *Chemical Society Reviews* **2016**, *45*, DOI: 10.1039/c6cs00135a.
- (39) Yang, X.-Y.; Chen, L.-H.; Li, Y.; Rooke, J. C.; Sanchez, C.; Su, B.-L. *Chem. Soc. Rev.* **2017**, *46*, 481–558.
- (40) Cho, C.-Y.; Moon, J. H. *Advanced Materials* **2011**, *23*, 2971–2975.
- (41) Hwang, D.; Lee, H.; Jang, S.-Y.; Jo, S. M.; Kim, D.; Seo, Y.; Kim, D. Y. *ACS Applied Materials & Interfaces* **2011**, *3*, 2719–2725.
- (42) Zhou, X.; Chen, H.; Sun, Y.; Zhang, K.; Fan, X.; Zhu, Y.; Chen, Y.; Tao, G.; Shi, J. *Applied Catalysis B: Environmental* **2014**, *152*, 271–279.
- (43) Loeh, M.; Badaczewski, F.; von der Lehr, M.; Ellinghaus, R.; Dobrotka, S.; Metz, J.; Smarsly, B. *Carbon* **2018**, *129*, 552–563.
- (44) Marcos-Hernández, M.; Villagrán, D., *11 - Mesoporous Composite Nanomaterials for Dye Removal and Other Applications*; Kyzas, G. Z., Mitropoulos, A. C., Eds.; *Micro and Nano Technologies*; Elsevier: 2019, pp 265–293.
- (45) Zhao, B. **2012**.
- (46) Thompson, B. R.; Horozov, T. S.; Stoyanov, S. D.; Paunov, V. N. *J. Mater. Chem. A* **2019**, *7*, 8030–8049.
- (47) Yuan, Z.-Y.; Su, B.-L. *J. Mater. Chem.* **2006**, *16*, 663–677.
- (48) Lopez-Orozco, S.; Inayat, A.; Schwab, A.; Selvam, T.; Schwieger, W. *Advanced Materials* **2011**, *23*, 2602–2615.
- (49) Yang, P.; Deng, T.; Zhao, D.; Feng, P.; Pine, D.; Chmelka, B. F.; Whitesides, G. M.; Stucky, G. D. *science* **1998**, *282*, 2244–2246.

- (50) Parlett, C. M.; Wilson, K.; Lee, A. F. *Chemical Society Reviews* **2013**, *42*, 3876–3893.
- (51) Tang, J.; Salunkhe, R. R.; Liu, J.; Torad, N. L.; Imura, M.; Furukawa, S.; Yamauchi, Y. *Journal of the American Chemical Society* **2015**, *137*, 1572–1580.
- (52) Xiao, H.; Ai, Z.; Zhang, L. *The Journal of Physical Chemistry C* **2009**, *113*, 16625–16630.
- (53) Shaw, D. J., *1 - The colloidal state*, Fourth Edition; Shaw, D. J., Ed.; Butterworth-Heinemann: Oxford, 1992, pp 1–20.
- (54) He, Z.; Alexandridis, P. *Polymers* **2017**, *10*, 32.
- (55) McClements, D. J.; Jafari, S. M. *Advances in Colloid and Interface Science* **2018**, *251*, 55–79.
- (56) Goodarzi, F.; Zendehboudi, S. *The Canadian Journal of Chemical Engineering* **2019**, *97*, 281–309.
- (57) Zhang, T.; Sanguramath, R. A.; Israel, S.; Silverstein, M. S. *Macromolecules* **2019**, *52*, 5445–5479.
- (58) Cameron, N. R., *Chapter 12 - Polymerized High Internal Phase Emulsion Monoliths*; Švec, F., Tennikova, T. B., Deyl, Z., Eds.; *Journal of Chromatography Library*, Vol. 67; Elsevier: 2003, pp 255–276.
- (59) Li, X.; Sun, G.; Li, Y.; Yu, J. C.; Wu, J.; Ma, G.-H.; Ngai, T. *Langmuir* **2014**, *30*, PMID: 24601731, 2676–2683.
- (60) Cameron, N. R.; Sherrington, D. C., *High internal phase emulsions (HIPes) — Structure, properties and use in polymer preparation*; Springer Berlin Heidelberg: Berlin, Heidelberg, 1996, pp 163–214.
- (61) Ikem, V.; Menner, A.; Bismarck, A. *Angewandte Chemie International Edition* **2008**, *47*, 8277–8279.
- (62) Capron, I.; Cathala, B. *Biomacromolecules* **2013**, *14*, PMID: 23289355, 291–296.
- (63) Tan, H.; Sun, G.; Lin, W.; Mu, C.; Ngai, T. *ACS Applied Materials & Interfaces* **2014**, *6*, PMID: 25102954, 13977–13984.
- (64) Alexandridis, P.; Hatton], T. A. *Colloids and Surfaces A: Physicochemical and Engineering Aspects* **1995**, *96*, 1–46.
- (65) Braun, S. *Comprehensive Biomaterials* **2011**, *4*, 529–543.
- (66) Bahman, F.; Elkaissi, S.; Greish, K.; Taurin, S., *Chapter 8 - Polymeric Micelles in Management of Lung Cancer*; Kesharwani, P., Ed.; Academic Press: 2019, pp 193–216.

- (67) Kunii, R.; Onishi, H.; Machida, Y. *European Journal of Pharmaceutics and Biopharmaceutics* **2007**, *67*, 9–17.
- (68) Santander-Ortega, M.; Jódar-Reyes, A.; Csaba, N.; Bastos-González, D.; Ortega-Vinuesa, J. *Journal of colloid and interface science* **2006**, *302*, 522–9.
- (69) Pitto-Barry, A.; Barry, N. P. E. *Polym. Chem.* **2014**, *5*, 3291–3297.
- (70) Kurahashi, M.; Kanamori, K.; Takeda, K.; Kaji, H.; Nakanishi, K. *RSC Adv.* **2012**, *2*, 7166–7173.
- (71) Valle, J. W.; Armstrong, A.; Newman, C.; Alakhov, V.; Pietrzynski, G.; Brewer, J.; Campbell, S.; Corrie, P.; Rowinsky, E. K.; Ranson, M. *Investigational new drugs* **2011**, *29*, 1029–1037.
- (72) Batrakova, E. V.; Kabanov, A. V. *Journal of Controlled Release* **2008**, *130*, Fifth International Nanomedicine and Drug Delivery Symposium, 98–106.
- (73) Escobar-Chávez, J.; López-Cervantes, M.; Naik, A.; Kalia, Y.; Quintanar, D.; Ganem, A. *Journal of pharmacy pharmaceutical sciences : a publication of the Canadian Society for Pharmaceutical Sciences, Société canadienne des sciences pharmaceutiques* **2006**, *9*, 339–58.
- (74) Dunphy, D. R.; Sheth, P. H.; Garcia, F. L.; Brinker, C. J. *Chemistry of Materials* **2015**, *27*, 75–84.
- (75) Galarneau, A.; Sachse, A.; Said, B.; Pelisson, C.-H.; Boscaro, P.; Brun, N.; Courtheoux, L.; Olivi-Tran, N.; Coasne, B.; Fajula, F. *Comptes Rendus Chimie* **2016**, *19*, Emerging Chemistry in France, 231–247.
- (76) Li, Y.; Chen, S.; Cai, X.; Hong, J.; Wu, X.; Xu, Y.; Zou, J.; Chen, B. H. *J. Mater. Chem. A* **2018**, *6*, 5695–5702.
- (77) Ganai, A. K.; Kumari, S.; Sharma, K. P.; Panda, C.; Kumaraswamy, G.; Gupta, S. S. *Chem. Commun.* **2012**, *48*, 5292–5294.
- (78) Cabaud, C.; Barré, Y.; De Windt, L.; Grandjean, A. *Separation and Purification Technology* **2019**, *229*, 115796.
- (79) Panda, C.; Ghosh, M.; Panda, T.; Banerjee, R.; Sen Gupta, S. *Chem. Commun.* **2011**, *47*, 8016–8018.
- (80) Pidko, E.; Hensen, E., *Computational Chemistry of Zeolite Catalysis*, 2016, pp 111–135.
- (81) Smit, B. *Chemical Reviews* **2008**, *108*, PMID: 18817356, 4125–4184.
- (82) Svelle, S.; Tuma, C.; Rozanska, X.; Kerber, T.; Sauer, J. *Journal of the American Chemical Society* **2009**, *131*, PMID: 19099476, 816–825.



- (83) Li, J.-R.; Kuppler, R. J.; Zhou, H.-C. *Chemical Society Reviews* **2009**, *38*, 1477–1504.
- (84) Giannozzi, P et al. *Journal of Physics: Condensed Matter* **2017**, *29*, 465901.
- (85) Hafner, J. *Journal of Computational Chemistry* **2008**, *29*, 2044–2078.
- (86) Evans, J. D.; Fraux, G.; Gaillac, R.; Kohen, D.; Trouselet, F.; Vanson, J.-M.; Coudert, F.-X. *Chemistry of Materials* **2017**, *29*, 199–212.
- (87) Cao, F.; Jing, Z.; Sun, H. *Adsorption Science & Technology* **2016**, *34*, 110–122.
- (88) Ramirez, I; Alcala, L.; Montoya, J. *Journal of Physics: Conference Series* **2019**, *1219*, 012019.
- (89) Mankad, V.; Jha, P. *AIP Advances* **2016**, *6*, 085001.
- (90) CEPAL DIAGNÓSTICO DE LAS ESTADÍSTICAS DEL AGUA EN ECUADOR, <https://aplicaciones.senagua.gob.ec/servicios/descargas/archivos/download/Diagnostico%20de%20las%20Estadisticas%20del%20Agua%20Producto%20IIIc%202012-2.pdf>, 2012.
- (91) INEC Medición de los indicadores de Agua, Saneamiento e Higiene (ASH), en Ecuador, <https://www.ecuadorencifras.gob.ec/documentos/web-inec/EMPLEO/2019/Indicadores%20DS%20Agua%2C%20Saneamiento%20e%20Higiene-2019/3.%20Principales%20resultados%20indicadores%20ASH%202019.pdf>, 2019.
- (92) Carlowicz, M. ‘Seasonal Pump’ Moves Water Between Ocean and Aquifers, <https://www.whoi.edu/oceanus/feature/seasonal-pump-moves-water-between-ocean-and-aquifers/>, 2005.
- (93) Momtaz, H.; Dehkordi, F. S.; Rahimi, E.; Asgarifar, A. *BMC public health* **2013**, *13*, 556.
- (94) Del Ambiente y Agua, M. Nueva estructura del Ministerio del Ambiente y Agua está lista, <https://www.ambiente.gob.ec/nueva-estructura-del-ministerio-del-ambiente-y-agua-esta-lista/>, 2020.
- (95) Ambiental, N. *Libro VI Anexo* **2014**, *1*.
- (96) INEN, N. *Norma Técnica Ecuatoriana. Instituto Ecuatoriano de Normalización. Agua potable. Requisitos. 5ta revisión. Quito-Ecuador* **2014**.
- (97) Sommer-Marquez, A.; Mansas, C.; Talha, N.; Rey, C.; Causse, J. *RSC Adv.* **2016**, *6*, 73475–73484.
- (98) Vernon-Parry, K. *III-Vs Review* **2000**, *13*, 40–44.

- (99) Leonard, D. N.; Chandler, G. W.; Seraphin, S., *Scanning Electron Microscopy*; American Cancer Society: 2012, pp 1–16.
- (100) Mohammed, A. **2018**.
- (101) Inkson, B., *2 - Scanning electron microscopy (SEM) and transmission electron microscopy (TEM) for materials characterization*; Hübschen, G., Altpeter, I., Tschuncky, R., Herrmann, H.-G., Eds.; Woodhead Publishing: 2016, pp 17 –43.
- (102) Landis, E. N.; Keane, D. T. *Materials Characterization* **2010**, *61*, 1305 –1316.
- (103) Wildenschild, D.; Sheppard, A. P. *Advances in Water Resources* **2013**, *51*, 35th Year Anniversary Issue, 217 –246.
- (104) Lin, A. S.; Stock, S. R.; Guldberg, R. E., *Microcomputed Tomography*; Hawkes, P. W., Spence, J. C. H., Eds.; Springer International Publishing: Cham, 2019, pp 2–2.
- (105) Microphotonics (Bruker today introduced the SkyScan 2211 Nano-CT), <https://www.microphotonics.com/bruker-skyscan-2211/>, 2016.
- (106) Cullity, B.; Stock, S., *Elements of X-ray Diffraction, Third Edition*; Prentice-Hall: 2001.
- (107) scope, M. X-Rays, <https://myscope.training/legacy/xrd/background/concepts/xrays/>, 2014.
- (108) Donald L. Pavia Gary M. Lampman, G. S. K.; Vyvyan, J. R., *Introduction to spectroscopy*; Cengage Learning: 2019; Vol. 5, pp 14–24.
- (109) Subramanian, A.; Rodriguez-Saona, L., *Chapter 7 - Fourier Transform Infrared (FTIR) Spectroscopy*; Sun, D.-W., Ed.; Academic Press: San Diego, 2009, pp 145 –178.
- (110) Larkin, P., *Chapter 3 - Instrumentation and Sampling Methods*; Larkin, P., Ed.; Elsevier: Oxford, 2011, pp 27 –54.
- (111) Elmer, P. *Technical note* **2005**, 27.
- (112) Glassford, S. E.; Byrne, B.; Kazarian, S. G. *Biochimica et Biophysica Acta (BBA) - Proteins and Proteomics* **2013**, 1834, 2849 –2858.
- (113) Ferrer, N., *Forensic Science, Applications of IR Spectroscopy*; Lindon, J. C., Ed.; Elsevier: Oxford, 1999, pp 603 –615.
- (114) Bunaciu, A. A.; Fleschin, Aboul-Enein, H. *Applied Spectroscopy Reviews* **2011**, *46*, 251–260.
- (115) Blitz, J. P., *Diffuse reflectance spectroscopy*; John Wiley & Sons New York: 1998; Vol. 14.

- (116) Technologies, P. **2017**.
- (117) Trunschke, A. (Diffuse Reflectance Spectroscopy in Heterogeneous Catalysis), [http://www.fhi-berlin.mpg.de/acnew/departament/pages/teaching/pages/teaching\\_\\_wintersemester\\_\\_2016\\_2017/annette\\_trunschke\\_\\_diffuse\\_reflectance\\_spectroscopy\\_\\_161111.pdf](http://www.fhi-berlin.mpg.de/acnew/departament/pages/teaching/pages/teaching__wintersemester__2016_2017/annette_trunschke__diffuse_reflectance_spectroscopy__161111.pdf), 2016.
- (118) Giannozzi, P. et al. *Journal of Physics: Condensed Matter* **2009**, *21*, 395502 (19pp).
- (119) Prandini, G.; Marrazzo, A.; Castelli, I. E.; Mounet, N.; Marzari, N. *npj Computational Materials* **2018**, *4*, 1–13.
- (120) Marsman, M; Marzari, N; Nitzsche, U; Nordstrom, L; Ozaki, T; Paulatto, L; Pickard, C.; Poelmans, W; Probert, M.; Refson, K, et al. *Science* **2016**, *351*, 6280.
- (121) Kokalj, A. *Journal of Molecular Graphics and Modelling* **1999**, *17*, 176–179.
- (122) Adhikari, A.; Chhetri, V. S.; Camas, A. *Journal of Food Protection* **2020**, *83*, 249–255.
- (123) Yu, A.; Loo, J. F.-C.; Yu, S.; Kong, S; Chan, T.-F. *Applied microbiology and biotechnology* **2013**, *98*, DOI: 10.1007/s00253-013-5377-9.
- (124) Sachse, A.; Galarneau, A.; Fajula, F.; Di Renzo, F.; Creux, P.; Coq, B. *Microporous and Mesoporous Materials* **2011**, *140*, 58–68.
- (125) Musi, S.; Filipovi-Vincekovi, N.; Sekovani, L. *Brazilian Journal of Chemical Engineering* **2011**, *28*, 89–94.
- (126) Garc a Ruiz, M.; Aguilar Pliego, J.; Nore  Franco, L. E.; M rquez  lvarez, C.; P  Pariente, J. A.-n.; Martin Guaregua, N. C. *Journal of applied research and technology* **2018**, *16*, 511–523.
- (127) Bala, T.; Gunning, R.; Venkatesan, D. M.; Godsell, J.; Roy, S.; Ryan, K. *Nanotechnology* **2009**, *20*, 415603.
- (128) Fornasieri, G.; Aouadi, M.; Durand, P.; Beaunier, P.; Riviere, E.; Bleuzen, A. *Chem. Commun.* **2010**, *46*, 8061–8063.
- (129) Mart nez, J.; Palomares-S nchez, S; Ortega-Zarzosa, G; Ruiz, F.; Chumakov, Y. *Materials letters* **2006**, *60*, 3526–3529.
- (130) Sudha, V; Ganesan, S.; Pazhani, G.; Ramamurthy, T.; Nair, G; Venkatasubramanian, P. *Journal of health, population, and nutrition* **2012**, *30*, 17–21.
- (131) Padil, V.; Cernik, M. *International journal of nanomedicine* **2013**, *8*, 889–98.
- (132) Sundar, S.; Venkatachalam, G.; Kwon, S. J. *Nanomaterials* **2018**, *8*, 823.
- (133) Fu, Z.; Zhou, S.; Yu, Y.; Zhang, S. *Chemical Physics Letters* **2004**, *395*, 285–289.

- (134) Parvulescu, V., *Catalytic Behavior of Metal Active Sites From Modified Mesoporous Silicas in Oxidation of Organic Compounds*, 2019.
- (135) Delahaye, E.; Moulin, R.; Aouadi, M.; Trannoy, V.; Beaunier, P.; Fornasieri, G.; Bleuzen, A. *Chemistry – A European Journal* **2015**, *21*, 16906–16916.
- (136) Chao, K. J.; Wu, C. N.; Chang, H.; Lee, L. J.; Hu, S.-f. *The Journal of Physical Chemistry B* **1997**, *101*, 6341–6349.
- (137) Todorova, S.; Pârvulescu, V.; Kadinov, G.; Tenchev, K.; Somacescu, S.; Su, B.-L. *Microporous and Mesoporous Materials* **2008**, *113*, 22–30.
- (138) Ágnes Szegedi; Kónya, Z.; Méhn, D.; Solymár, E.; Pál-Borbély, G.; Horváth, Z. E.; Biró, L. P.; Kiricsi, I. *Applied Catalysis A: General* **2004**, *272*, 257–266.
- (139) Sohrabnezhad, S.; Valipour, A. *Spectrochimica Acta Part A: Molecular and Biomolecular Spectroscopy* **2013**, *114*, 298–302.
- (140) Kucherov, A.; Shigapov, A.; Ivanov, A.; Kucherova, T.; Kustov, L. *Catalysis Today* **2005**, *110*, First International Workshop on the Application of Microporous and Mesoporous Materials as Catalytic Hosts for Fe, Cu and Co, 330–338.
- (141) Evarestov, R. A.; Veryazov, V. A. *physica status solidi (b)* **1990**, *158*, 201–212.
- (142) Wu, H.; Desai, S. R.; Wang, L.-S. *The Journal of Physical Chemistry A* **1997**, *101*, 2103–2111.
- (143) Davydova, L.; Boreskov, G.; Popovskii, V.; Yurieva, T.; Anufrienko, V. *Reaction Kinetics and Catalysis Letters* **1982**, *18*, 203–207.
- (144) Laskowski, L.; Laskowska, M.; Fijalkowski, K.; Piech, H.; Jelonkiewicz, J.; Jaskulak, M.; Gnatowski, A.; Dulski, M. *Journal of Nanomaterials* **2017**, 2017, DOI: 10.1155/2017/1287698.